12

Radiative properties of the terrestrial 'surface–atmosphere' system

The purpose of the present chapter is to consider and analyse some directions of microwave remote sensing being actively developed at present by the researchers in various science teams. The solutions of the equation of the transfer theory for a homogeneous layer of a gaseous-disperse medium are considered as a methodological basis for detailed study of the hydrometeorological parameters of the terrestrial atmosphere. The results of ground-, aircraft- and space-based observations and monitoring of integral parameters of the water vapour content of the atmosphere and thermodynamic temperature profiles are presented. The results of analysing the contribution of microwave measurements into classification schemes of recognizing various types of cloudy systems are given. The chapter also presents the basic results of observation of the wavy sea surface by microwave radiothermal aircraft- and space-based complexes, including situations with breakings of sea waves and vast oil spillage.

12.1 RADIATION OF THE HOMOGENEOUS OCEAN–ATMOSPHERE SYSTEM

Numerical integrations of the radiative transfer equation for the atmosphere–ocean system in the microwave frequency band on the basis of equations (9.64)–(9.66) were performed by a variety of authors (Wilheit and Fowler, 1977; Tsang *et al.*, 1977; Wilheit and Chang, 1980; Mitnik, 1986; Sasaki *et al.*, 1987; Liebe, 1989; Kotlyar and Khapin, 1990; Matzler, 1992, 2000).

12.1.1 The basis model

This spatio-homogeneous model, which was described in detail by Mitnik (1986), enables one to estimate the influence of hydrometeorological parameters and viewing

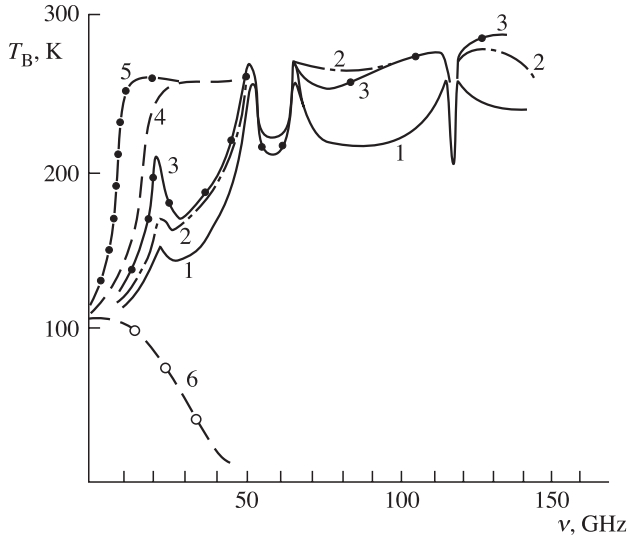

Figure 12.1. Qualitative microwave spectra of the brightness temperature for the ocean–atmosphere system in sensing at the nadir with a satellite: (1) standard cloudless atmosphere; (2) clouded atmosphere: $Q = 0.38\,\mathrm{kg\,m^2}$; (3) tropical atmosphere; (4) rain cloud at $5\,\mathrm{mm\,h^{-1}}$; (5) rain cloud at $25\,\mathrm{mm\,h^{-1}}$; (6) contribution of surface emission.

angle θ variations on the brightness temperatures $T_B(\nu, \theta)$ for horizontal (H) and vertical (V) polarizations in the frequency range of 0.5–300 GHz.

The examples of calculated $T_B(\nu, \theta)$ spectra for microwave emission of the atmosphere–ocean system with a smooth sea surface (at 35‰ salinity) using equations (9.64)–(9.66) under standard gaseous cloudless atmosphere (curve 1), standard cloudy atmosphere (total cloud water content $Q = 0.39\,\mathrm{kg/m^2}$ at $t = -10^{\circ}\mathrm{C}$) (curve 2), tropical atmosphere (curve 3) and rain cloud conditions (curves 4 and 5) are presented in Figure 12.1.

Initially it should be pointed out, that, first, the distinctive properties of emission spectra are observed for the standard and tropical atmosphere in the ranges of 20–40 and 80–110 GHz, and, second, the brightness temperature sharply decreases in the ranges of strong gaseous oxygen absorption (the band of 55–65 GHz and the strong line at 118 GHz). These features are determined from the temperature profile properties and from the peculiarities of the oxygen weighting function. So, Figures 12.2 and 12.3 show the detailed spectra of brightness temperature of the atmosphere – ocean system for the strong oxygen line of 118 GHz and the normalized weighting functions (see equation (9.64)) for various working frequencies in the frequency range of 115–118.7 GHz (Kotlyar and Khapin, 1990). The odd-shaped spectra of the 118 GHz line have attracted our attention with respect to the standard temperature profile (curve 1), the summer arctic temperature profile (curve 2) and the tropical profile (curve 3). Figure 12.3 shows that radio-emission in the frequency band of 115–117 GHz is formed at altitudes of 0–8 km (curves 1 and 2).

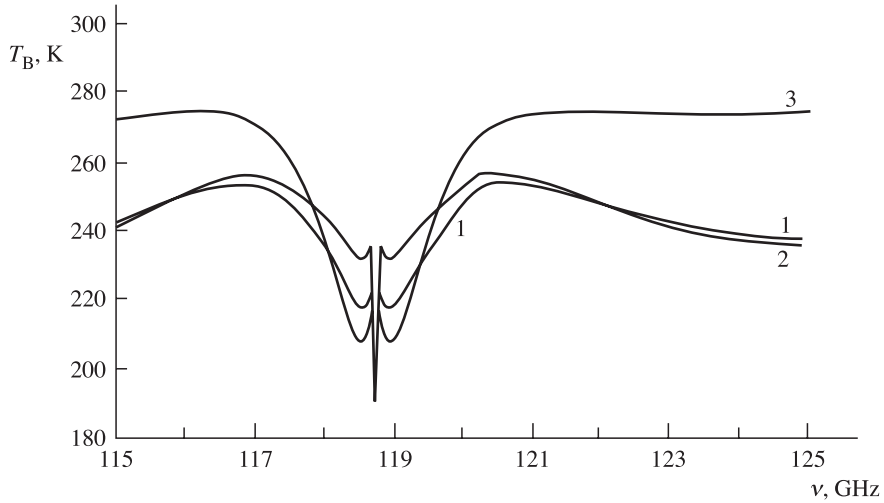

Figure 12.2. Spectra of the brightness temperature for the ocean–atmosphere system in sensing at the nadir with a satellite at frequency range 115–125 GHz (Kotlyar and Khapin, 1990).

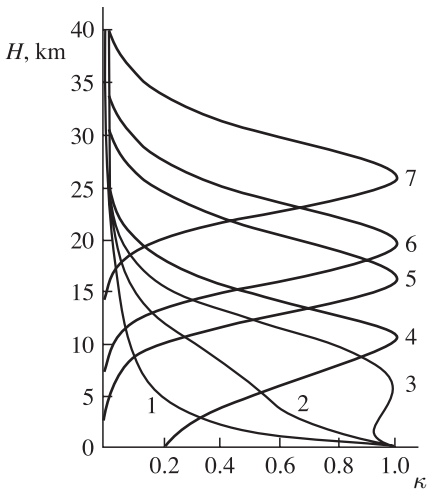

Figure 12.3. Normalized weighting functions $\kappa(H)$ in sensing at the nadir with a satellite at frequency range 115–118.5 GHz (Kotlyar and Khapin, 1990).

The weighting functions for the band of 117–118.5 GHz are characterized by a sharp decrease of emissivity and possess maximum values at altitudes of 5–16 km (curves 3–5). The minimum brightness temperature values at about 118.5 GHz are derived from the fact that the emission at these frequencies is formed in the tropopause (12–25 km) area, where very low temperatures prevail. Radio-emission in the frequency range of 118.5–118.7 GHz is formed in the terrestrial stratosphere

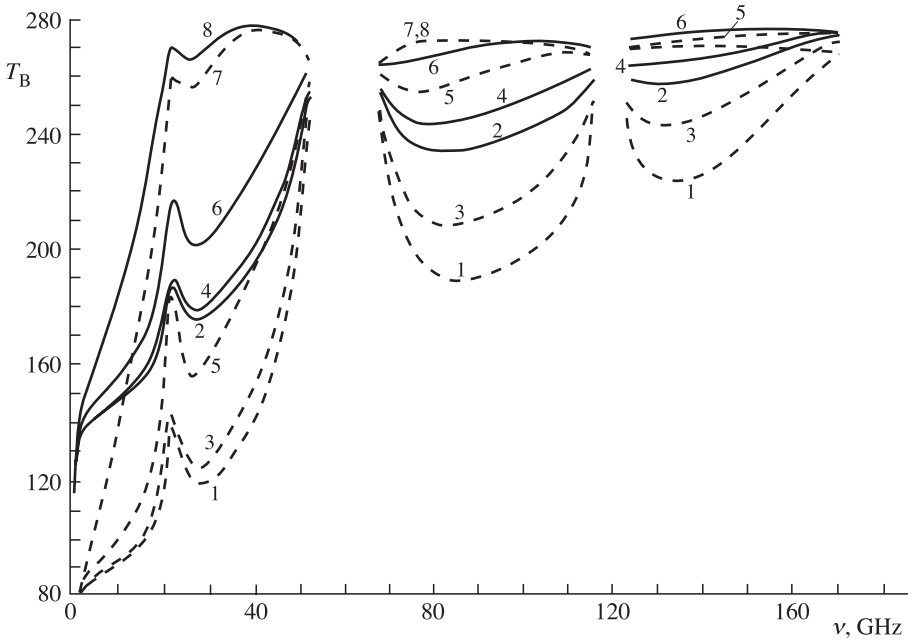

Figure 12.4. Theoretical spectra of the brightness temperature for the ocean–atmosphere system at microwave frequency range. Dashed and solid lines represent respectively the horizontal and vertical polarization signals. See notation in the text (Mitnik, 1986).

where the temperature increases with altitude (curves 6 and 7). So, the radioemission received by radioset channels at frequencies in the band of 115–118.5 GHz carries useful information about the thermodynamic temperature profile in the altitude layer from 0 to 30 km.

The model examples of calculated spectra for horizontal and vertical polarization ($\theta = 45^\circ$) with $\nu = 1$–170 GHz are presented in Figure 12.4 (Mitnik, 1986). In the standard cloudless atmosphere (curves 1 and 2) the total water vapour content is $V = 1.3\,\mathrm{g/cm^2}$. The cloudiness of stratified forms (St., Sc., curves 3 and 4) are characterized by the following parameters: $Q = 0.1\,\mathrm{kg/m^2}$, $t = +10^\circ\mathrm{C}$, $V = 1.3\,\mathrm{g/cm^2}$. In the case of cumuli of medium vertical development (Cu med., curves 5 and 6) $Q = 0.5\,\mathrm{kg/m^2}$, $t_C = +10^\circ\mathrm{C}$, $V = 5.1\,\mathrm{g/cm^2}$. For heavy cumuli at $\nu > 40$ GHz the distinctions in polarization are very small due to the increase in optical thickness in the sensing direction.

First of all, we shall consider cloudiness with small and mean values of the total liquid water content ($Q < 0.5\,\mathrm{kg/m^2}$). From the analysis of numerical experimental data it follows that maximum variations of the brightness temperatures, stipulated by alterations in cloudiness parameters, are noticed over the ranges of ~25–50, ~70–113 and ~125–170 GHz. At $Q = 0.1$–$0.3\,\mathrm{kg/m^2}$ and $t_C = -10$ to $+10^\circ\mathrm{C}$ (which is natural for the clouds of St., Sc., Ac, As Cu hum) the brightness contrast of cloudy areas against the cloudless background

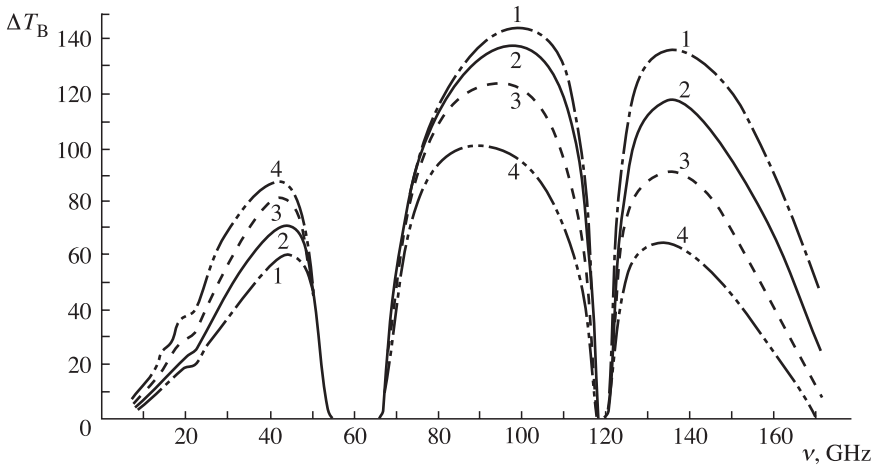

Figure 12.5. Theoretical spectra of partial derivatives of the brightness temperature of a clouded atmosphere with total cloud liquid water content at low Q values: (1) $t_C = +10°C$; (2) $t_C = 0°C$; (3) $t_C = -10°C$; (4) $t_C = -20°C$ (Mitnik, 1986).

$\Delta T_B(\nu, t) = T_{BC}(\nu, t) - T_B(\nu)$ is observed in the nadir direction: 3–25 K at $\nu = 25$–50 GHz, ~10–40 K at $\nu = 75$–110 GHz and ~5–35 K at $\nu = 125$–155 GHz. For sensing at the angle of 45° for horizontal polarization the corresponding contrast will grow up to ~6–40, ~15–55 and ~7–45 K.

The sensitivity of the brightness temperature of the atmosphere–ocean system to the cloudiness parameters variation can be characterized by partial derivatives spectra $\alpha(\nu) = T_B(\nu)/Q$ and $\beta(\nu) = T_B(\nu, t)/t_C$.

In the range of $\nu < 53$ GHz the $\alpha(\nu)$ derivative grows monotonously with frequency up to the maximum at $\nu = 43$–45 GHz; then it is followed by decreasing owing to the oxygen absorption increase (Figure 12.5). The temperature drop from +10 to 20°C is accompanied by its increasing by a factor of about 1.6–2.2 depending on the frequency. At $\nu = 43$ GHz the $\alpha(\nu)$ values are equal to 60 K/(kg/m^2) at $t_C = +10°C$ and 87 K/(kg/m^2) at $t_C = -20°C$.

At measurements with $\theta = 45°$ the values of α for vertical polarization are roughly the same as with $\theta = 0°$ (nadir), and for horizontal polarization they are about 1.5–1.6 times greater.

In the transparency window of 70–115 GHz the brightness contrasts and the values of the $\alpha(\nu)$ derivative are weaker as compared to lower frequencies, at positive temperatures particularly. The change of the derivative sign from negative to positive is an important distinctive feature. The maximum values of $\alpha(\nu)$ at $\theta = 0°$ may be as great as 100–140 K/(kg/m^2) in accordance with t_C and fall within the spectral range of 87 to 100 GHz. At $\theta = 45°$ the $\alpha(\nu)$ values increase by a factor of 1.4–1.6 for horizontal polarization and decrease by about 25% for vertical polarization.

In the frequency band of 125–170 GHz the maximum values of derivatives are lower than those at $\nu = 70$–115 GHz, the difference increasing as the temperature

drops. This results from the cumulative effect of cloud and water vapour absorption spectra and from increasing sea surface emissivity.

12.1.2 Integral parameters

The analysis of spectral dependencies of the gaseous-disperse medium of the atmosphere shows that the use of the data of measurements of microwave radiation in the centimetre and millimetre bands has many significant advantages as compared to using the data of measurements in the infrared and optical bands for similar purposes. The basic feature of microwave radiation in the 3 cm – 1 mm band is its high informative capacity, which is caused by a strong dependence of radiation intensity on hydrometeorological parameters of the atmosphere and on its gaseous components in the semi-transparent medium regime (Chapters 10 and 11). And in this case for a number of physical characteristics of the studied medium (the water vapour content of the atmosphere, the liquid water content of clouds, the rates of liquid and solid precipitation, the content of minor gaseous components) the variations of microwave radiation are about linearly related with the values of integral parameters of the gaseous-disperse atmosphere. This allows one to essentially simplify the procedures of restoring physical parameters from the data of remote microwave measurements. It is for just these reasons that this band has attracted the close attention of researchers from the very beginning of the active phase of purposeful remote investigations of thermal radiation of the ocean–atmosphere system in 1968–1972 (Basharinov *et al.*, 1969, 1971, 1973; Staelin, 1969; Akvilonova *et al.*, 1971, Mitnik, 1972; Rosenkranz *et al.*, 1972) up to the most recent time (Gasiewski and Johnson, 1993; Abbas *et al.*, 1996; Hartmann *et al.*, 1996; Bartsch *et al.*, 1996; Wang *et al.*, 1997a, b, c; Mitnik and Mitnik, 2003; Raffalski *et al.*, 1998; Karmalkar *et al.*, 2002; Lohnert and Crewell, 2003). Apparently this tendency will be maintained in the future as well.

Now we shall demonstrate the advantages of this band proceeding from the results we have obtained earlier (Chapters 10 and 11). So, the radiobrightness temperature of downward radiation of the semi-transparent gaseous-disperse atmosphere at upward-looking measurements can be presented as

$$T_{\mathrm{B}}(\nu) = [T_0 - \Delta T(\nu)][\tau_{\mathrm{G}}(\nu) + \tau_{\mathrm{D}}(\nu)] \operatorname{cosec} \theta, \tag{12.1}$$

where $t_{\mathrm{G}}(\nu)$ and $t_{\mathrm{D}}(\nu)$ are optical paths of gaseous and disperse components of the atmosphere, respectively (see relations (11.74)). Similar relations can also be obtained for upward radiation with allowance for re-emission of a studied layer from the surface (see relations (9.69) and (9.74)). Since the optical path value is an integral characteristic both for gaseous components (see relation (11.85)), and for disperse components (see relation (10.71)), the brightness temperature $T_{\mathrm{B}}(\nu)$, measured at different frequencies ν_i, can be presented by a fairly simple regression relation

$$T_{\mathrm{B}}(\nu_i) = a_0(\nu_i) + \sum a_j(\nu_i) P_j, \tag{12.2}$$

where P_j are unknown integral parameters of gaseous and disperse media of the

atmosphere and, first of all, the water vapour content of the atmosphere V (kg/m^2) the liquid water content of clouds Q (kg/m^2), the liquid and solid precipitation rates, and the content of minor gaseous components (ozone, chlorine oxide and other gases). The electromagnetic properties of disperse systems are considered in the Rayleigh approximation in this case. The $a_j(\nu_i)$ coefficients are usually found by the least-squares method under monitored conditions when remote observations of seasonal, latitudinal and geographical features are performed. To solve a very important problem of separating the components bound with water vapour and cloud liquid-water content, the two-channel ($i = 2$) technique was proposed earlier for determining the total vapour content and total cloud liquid-water content. This technique has used the measurements at the frequency close to the frequency of the first strong water vapour transition (22.235 GHz) and at the frequency chosen in the transparency window, but with a strong dependence on a disperse-drop phase (the band of 28–32 GHz). Using (12.2), we obtain in this case:

$$V = A_{0V} + A_{1V}T_B(\nu_1) + A_{2V}T_B(\nu_2), \tag{12.3}$$

$$Q = A_{0Q} + A_{1Q}T_B(\nu_1) + A_{2V}T_B(\nu_2). \tag{12.4}$$

Theoretically, the optimal choice of frequencies for the two-frequency algorithm is considered to be as follows: the central transition frequency is $\nu_1 = 22.235$ GHz and frequency $\nu_2 = 31.4$ GHz. This choice of frequencies, which ensures the maximum signal-to-noise ratio at measurements, suggests a constancy of pressure and temperature profile. In practical observations, where the pressure and temperature are variable quantities, this choice is not optimal. Depending on the local position latitude (the arctic region, middle latitudes, tropics), on the observation time and on hydrometeorological features of the region, the choice of observation frequencies can vary (Wang *et al.*, 1992; Karmalkar *et al.*, 2002). A principal step in the further development of this algorithm is the introduction of additional channels in the transparency window of 90 GHz and in the line of 183 GHz, which allows one to essentially improve the retrieval accuracy of the total cloud liquid-water content (Matzler, 1992; Wang *et al.*, 1992; Lohnert and Crewell, 2003; Weng *et al.*, 2003).

At present, there exists a variety of both ground complexes in various latitudinal belts, and aircraft multifrequency systems for observation and monitoring of the total liquid-water content (of vapour and drops) in the atmosphere (Rosenkranz *et al.*, 1972, 1982; Rassadovsky and Troitsky, 1981; Amirkhanyn *et al.*, 1975; Wang *et al.*, 1994; English, 1995; Taylor and English, 1995; Antonov *et al.*, 1995; Wang *et al.*, 1997a; Skofronick-Jackson and Wang, 2000).

For space observations a similar algorithm was first utilized in processing the data from measuring the upward radiation of the ocean–atmosphere system by means of radiothermal multifrequency instruments installed on the 'Cosmos-243' satellite (1968). This complex included the channels of 0.8, 1.35, 3.2 and 8.5 cm. The measurements, carried out with this complex, made it possible to obtain for the first time statistically significant estimates of the content of water vapour (in the 1.35-cm channel), small-drop water (in the 0.8-cm channel) and liquid precipitation (in the 3.2-cm channel) over the oceans. The mean latitudinal distribution of total

humidity over the Pacific, Atlantic and Indian oceans was found to be similar. The measurements, carried out from September 23 till September 27 1968, have shown that about 0.7% of water in the terrestrial atmosphere is in the liquid-drop state (Basharinov *et al.*, 1969, 1974; Akvilonova *et al.*, 1971, 1973).

The next step was the launching of the 'Nimbus-6' satellite (1975) with radiothermal instruments working in frequency channels of 22.235 and 31.65 GHz for implementing the two-channel algorithm. This complex also included oxygen channels (at 52.85, 53.85 and 55.45 GHz) and polarization observations in the transparency window at the 37 GHz frequency.

The modern multifrequency space-based two-polarization microwave complexes (the Advanced Microwave Scanning Radiometre (AMSR) onboard the ADEOS-2 satellite and the Advanced Microwave Sensing Unit (AMSU) onboard the NOAA 15 and NOAA 16 satellites essentially expand the possibilities of microwave systems while keeping the two-channel algorithm as an integral part of the general measurement ideology. In addition, these systems allow one to retrieve not only the integral parameters of liquid-water content (in vapour and liquid phase), but also the sea surface temperature and the surface wind speed, and also to separate the total liquid-water content of a solid phase (ice) and the surface precipitation rates (Kidder *et al.*, 2000; Shibata, 2000; Weng *et al.*, 2003; Mitnik and Mitnik, 2003).

12.1.3 Temperature profiles

One of the most important problems in meteorology is the retrieval of temperature profiles of the atmosphere in the extended altitude interval from remote sensing data of measurements of downward (observations at the earth's surface) and upward (observations on flight vehicles) radiation fluxes. The investigations carried out over a long period of time have shown that the optimal procedure for solving this problem is remote sensing in the millimetre-wavelength band in spin-rotational lines of oxygen (see Chapter 11). The possibilities of using radiation of this particular atmospheric gas are related, on the one hand, with a high stability of the content of molecular oxygen in the atmosphere (as opposed to water vapour content), whose radiation intensity essentially depends on the thermodynamic temperature. And, on the other hand, in this band high-sensitivity radiospectrometres are implemented with spectral resolution ranging from thousands to units of megahertz, i.e. with $(\Delta\nu/\nu) \sim 10^{-4}$–$10^{-5}$. Such high resolutions in the passband of receiving systems of radiospectrometres (see Chapter 3) are necessary for selecting the radioemission coming from various layers of a studied gas medium. To better understand the physical basis of such kinds of measurements we shall make use of the solutions of the gas medium transfer equation for the microwave range given by equations (9.64) and (9.66). We shall rewrite these relations in a more general form

$$T_{\mathrm{B}}(\nu) = \int_0^{H_0} T(s)K(\nu, s)\,\mathrm{d}s, \tag{12.5}$$

where $K(\nu, s)$ is called the kernel of the equation, or a weighting function. Since

each elementary gas layer possesses absorption of the radiation of the preceding layers and, at the same time, emits its own energy, the general altitude form of a weighting function can be rather complicated and, depending on the chosen observation frequency, can possess an altitude maximum. In other words, there will exist a layer altitude at which the emission will be determining for the emission of the total column of gas. Thus, the radiospectrometric reception of radiation with high resolution makes it possible to select and retrieve the temperature profile. Various geometries of the experiment (as, for example, observations from the earth's surface or from flight vehicles) results, generally speaking, in various forms and values of weighting functions. One of examples of a set of weighting functions for the line of 118 GHz in observation from a spacecraft is presented in Figure 12.3. In observation from the earth's surface the boundary layer of the atmosphere is sensed at the frequency of 60 GHz up to altitudes of 0.5 km. Sensing at 53.5, 54.5 and 55 GHz frequencies provides information on the temperature regime of the troposphere. When sensing at frequencies of 53.0633 and 53.0668 GHz by means of high-resolution instruments $(\Delta\nu/\nu) \sim 10^{-5}$ one can obtain data on temperature distribution at altitudes of the order of 35–55 km (Naumov *et al.*, 1999). If the receiving device possesses a broad passband, of the order of $(\Delta\nu/\nu) \sim 0.05$–0.1, then the received signal will contain the integral-over-altitude information on weighted-mean temperature without discriminating the altitude profile.

From the mathematical point of view equation (12.5) represents the integral Fredholm equation of the first kind for determining the altitude profile of temperature. This problem relates to a scope ill-defined, in the classical sense, problems and requires special methods of solution (Tichonov and Arsenin, 1979; Naumov *et al.*, 1999).

Thus, radiothermal instruments for thermal sensing of various atmospheric altitudes are subdivided into three classes, in accordance with the physical conditions of forming radiation in oxygen spectral lines, namely:

- high-resolution spectral instruments (6–8 channels), $\Delta\nu \sim 1$–3 MHz, for remote sensing of the stratosphere and mesosphere in distinguishing resonances of the 5-mm band;
- medium-resolution spectral instruments (4 or 5 channels), $\Delta\nu \sim 200$–300 MHz, for troposphere sensing at the wing of the 5-mm absorption band in the range of 53–58 GHz;
- broadband single-channel radiometers, $\Delta\nu \sim 2$–4 GHz, for sensing the boundary layer of the atmosphere at the absorption band centre in the range of 58–62 GHz.

The radiothermal complexes for thermal sensing produced until now are situated both at stationary observation stations and on transportable platforms, and in a ship version (Ciotti *et al.*, 1987; Troitsky *et al.*, 1993; Antonov *et al.*, 1995; Raffalski *et al.*, 1998; Cimini *et al.*, 2003; Kadygrov *et al.*, 2003).

12.2 MICROWAVE REMOTE SENSING OF CLOUD FIELDS

Clouds play a crucial role in the earth's climate by having an influence on key parameters, such as the radiation budget, the heating of the earth's surface, and the diabatic heating of the atmosphere. They play a dual role on the top of the atmosphere radiation budget. In the short-wave region, clouds reflect the incoming radiation back to space, thereby decreasing the amount of solar energy available for absorption in the atmospheric column and at the surface. On the other hand, in the long-wave region they absorb the radiation emitted by the earth's surface and the lower atmosphere and re-radiate it to space at a lower temperature, thereby causing the greenhouse effect. The net effect of clouds is the sum of these two processes, and it depends on the type and amount of clouds present at any particular geographic region of interest. Therefore, in a broad sense the distribution of cloud type and amount determines the distribution of energy sources and sinks in the terrestrial atmosphere, and, hence, is important to the general circulation of the atmosphere (Palmen and Newton, 1969; Webster, 1994).

The importance of clouds in the tropical parts of the World Ocean to global climate arises from the impact of clouds on radiative fluxes, atmospheric latent heating, and the fresh water flux into the ocean. The impact of clouds on the earth's radiation balance and the distributions of cloud types and amounts have been a subject of many investigations (e.g., Marchuk *et al.*, 1986; Akilonova *et al.*, 1973; Akvilonova and Kutuza, 1978; Kutuza and Smirnov, 1980; Matveev *et al.*, 1986; Doviak and Zrnic, 1984; Cahalan, 1989; Houze, 1993; Davis *et al.*, 1996; Chang and Chiu, 1997; Kondratyev *et al.*, 1995; Liu *et al.*, 1995; JSTC, 1995; Arrault *et al.*, 1997; Meneghini *et al.*, 1997; Liu and Curry, 1998, 1999, 2000; Sharkov, 1998; Lin *et al.*, 1998a, b; Jameson *et al.*, 1998; Stephens *et al.*, 1998; IPCC, 2001; and references therein).

The results of a microscale cloud case study were presented by Intrieri *et al.* (1995) to illustrate the advantages of multi-wavelength observations. The combination of measurements from ground-based lidar (optic), radar (microwaves), interferometres and radiometers (microwaves) yield two-spatial geometrical, microphysical and radiative information not attainable by any one of these instruments alone.

There is no question that the potential satellite systems for investigations of fine cloud structures will carry multi-wavelength instruments. The role of microwave radiometry in the clouds project will be fundamental (Bizzari and Spera, 2000; Bizzari *et al.*, 2000).

12.2.1 Cloud classification schemes – the contribution of microwave radiometry

Different cloud types play different roles in the climate, with convective clouds providing the dominant contribution to precipitation and the layer clouds with their larger horizontal extent having a greater influence on radiative fluxes. Furthermore, the type of cloud associated with precipitation determines the impact of the precipitation on the tropical sea surface temperature and ocean mixed layer

characteristics. Deep convective precipitation is typically associated with strong surface winds, and the ensuing fresh water is easily mixed into the ocean below. By contrast, precipitation associated with shallow, isolated convection is generally accompanied by low wind speeds, resulting in the formation of a fresh water lens on the ocean surface that acts to stabilize the upper ocean and allows the sea surface temperature to warm (Webster, 1994; Webster and Lukas, 1992).

Therefore, the classification of cloud and precipitation regimes is very important to understanding the cloud effects on the earth's environment, particularly in the tropical oceans. Nevertheless, there is a lack of a universally accepted classification scheme of cloud systems. The most traditional approaches (schemes) consist in discrimination of the cloud fields via cloud-top height variations from infrared and visible cloud images by GMS, NOAA and Meteosat systems. Fuller data, based on visible and infrared radiances, are collected for the International Satellite Cloud Climatology Project (ISCCP) (see, for example Rossow and Schiffer, 1991; ISTC, 1995; IPCC, 2001) and by the Meteorological Satellite Center of Japan from GMS-IR data.

The classification of cloud types using combined infrared and visible satellite data typically uses the visible channel to provide information on cloud thickness and the infrared channel to provide information on the cloud-top height (Rossow and Schiffer, 1991). However, this approach does not allow one to infer the properties of deep clouds because of the saturation of both infrared and visible radiation. The large pixel-size and the lack of information regarding cloud height hamper cloud retrieval schemes that solely use satellite microwave data. To overcome the drawbacks associated individually with visible/infrared and microwave cloud retrieval schemes from satellite, a combined classification scheme was proposed by Liu *et al.* (1995) that uses combined infrared and microwave data. Using satellite microwave data also provides information on precipitation which cannot be obtained from the traditional infrared/visible classification schemes.

The proposed cloud classification scheme utilizes the cloud-top temperature obtained from infrared measurements (GMS-4) and a microwave index that is formed from special sensor microwave/imager (SSM/I) data of F-10 and F-11 DMSP satellites (see Chapter 14). The infrared data are used to determine the cloud-top temperature, and the microwave data are used to determine an index that includes both microwave scattering and emission. GMS infrared data are employed to separate cloudy from clear-sky pixels and to derive cloud-top temperature. A simple histogram–threshold method is used to determine cloudy pixels (Rossow and Schiffer, 1991).

The difference between cloud-top temperature and its brightness temperature should be smaller because of the thinner absorption layer above the cloud top than above the sea surface. The higher the cloud-top height, the smaller the difference. Accordingly, the cloud-top temperature, T_C, is calculated from the brightness temperature, T_{IR}, by the following equation:

$$T_C = T_{IR} + 8\left(\frac{T_{IR}}{150} - 1\right) \tag{12.6}$$

That is, the difference between T_C and T_{IR} is about 8 K near the sea surface (300 K) and decreases linearly as the cloud-top height increases.

A 'semi-empirical' 'microwave index' f is defined as follows to represent the strength of the microwave signal from a cloudy pixel:

$$f = \left(1 - \frac{D}{D_0}\right) + 2\left(1 - \frac{PCT}{PCT_0}\right), \tag{12.7}$$

where D represents the polarization at 19 GHz given by $D = T_{B19V} - T_{B19H}$, and T_{B19V} and T_{B19H} are, respectively, vertically and horizontally polarized brightness temperatures at 19 GHz; D_0 is D at the threshold for precipitation; PCT is the 85 GHz polarization-corrected temperature defined as $PCT = 1.818T_{B85V} - 0.818T_{B85H}$, and T_{B85V} and T_{B85H} are, respectively, vertically and horizontally polarized brightness temperatures at 85 GHz; and PCT_0 is PCT at the threshold for the onset of precipitation. The precipitation threshold is determined according to the rainfall algorithm, whereby the threshold is derived from the SSM/I data themselves for every $5 \times 5^\circ$ which includes climatological information. The first term on the right-hand side of (12.7) represents the microwave emission signal and the second term the scattering signal, so that index f accounts for both emission and scattering. Because the PCT rarely drops below 150 K, the maximum value of $(1 - PCT/PCT_0)$ is almost a half of the maximum value of $(1 - D/D_0)$. A factor of 2 is therefore given to the scattering term, so that the emission and the scattering terms have equal contributions to the microwave index function.

The rainfall algorithm includes the following features: (1) different formulas are used for non-precipitating and precipitating clouds; (2) a scheme for calculating clear-sky brightness temperature is included, which can easily be turned by observed SSM/I data, and the contribution of the components other than liquid water (i.e. the sea surface and atmosphere) can be remote without being biased; (3) the cloud mean temperature, to which the liquid water path retrieval is very sensitive, is derived from the SSM/I brightness temperature and cloud-top temperature determined from the infrared satellite data (GMS data in this case); and (4) the effects of precipitating-size water drops and ice particles and of the inhomogeneity of the rain field in a satellite footprint are accounted by combining 19 and 37 GHz measurements.

As shown by Liu *et al.* (1995), the microwave index f is a good indicator for rainfall rate and 'dense ice'. In addition, the cloud-top temperature is also used for cloud classification. Clouds are classified into eight classes based on the microwave index f and the GMS cloud-top temperature (Figure 12.6), namely: (1) a warm non-precipitating cloud, (2) a warm precipitating cloud, (3) a mid-top non-precipitating cloud, (4) a mid-top precipitating cloud, (5) a thin high-top non-precipitating cloud, (6) a deep high-top non-precipitating cloud, (7) an anvil with stratiform precipitating cloud, and (8) a deep convective precipitating cloud.

The classes defined are based primarily upon cloud physical considerations. The warm clouds have cloud-top temperatures warmer than 0°C. No ice-phase particles would be expected in these clouds. The mid-top clouds have cloud-top temperatures from 0 to −40°C, and the clouds in these categories could be of mixed phase (or

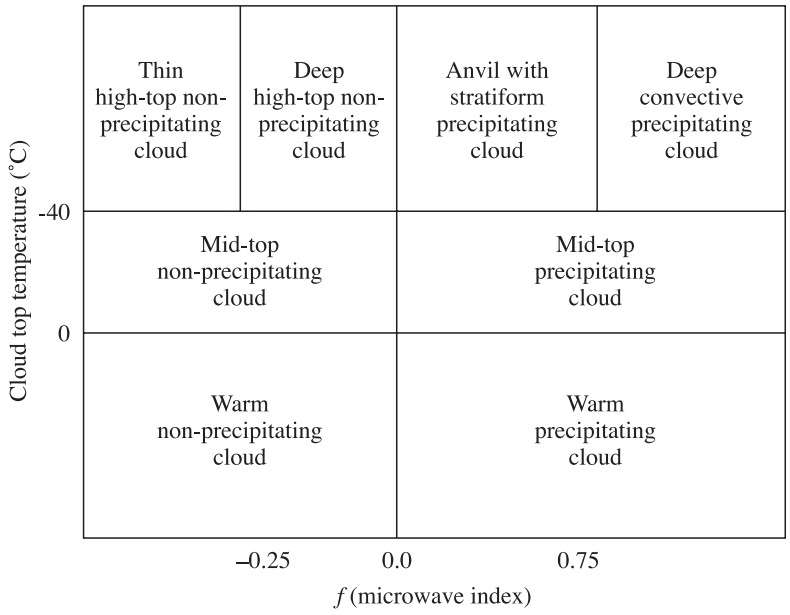

Figure 12.6. Schematic diagram of the microwave index f versus cloud top temperature for cloud classification (Liu *et al.*, 1995).

either phase). The cloud-top temperatures for the last four cloud types are colder than -40°C. Ice-phase particles can be easily observed in these clouds.

Precipitating and non-precipitating clouds are separated based on the value of the microwave index greater or less than zero. For clouds with tops colder than -40°C, four different cloud types are further defined. The thin, high-top, non-precipitating cloud, $f < 0.25$, has almost no liquid water. The deep, high-top, non-precipitating cloud has a liquid water path as large as about $150\,\mathrm{g/m^2}$, on the average, when $f = 0$. It could consist of several layers, perhaps, a liquid-water cloud layer underlying a cirrus deck, and rainfall is not detected.

Anvil with a stratiform precipitating cloud has a greater liquid water content and is precipitating. Besides, having a greater liquid water content and heavy rainfall rate, the most striking feature of deep convective precipitating cloud compared to anvil with stratiform precipitating cloud is that it contains a significant amount of 'dense ice'. As mentioned earlier, the ice water path from SSM/I only reflects the 'dense ice' particles with large size and densities, such as graupel. A strong updraft is required to produce and maintain the 'dense ice' in the cloud, which may only occur in deep convective clouds. Therefore, although the separation between anvil with stratiform precipitating cloud and deep convective cloud is based on cloud physical consideration, i.e. whether or not there is a significant amount of 'dense ice', it also reflects the difference in cloud dynamics for the two cloud types. It can be seen that the dense ice index is about $200\,\mathrm{g/m^2}$ at $f = 0.75$ (the boundary between anvil with stratiform precipitating cloud and deep convective cloud). The choice of $f = 0.75$

instead of $f = 0.5$ (where the ice index is equal to 0) is based on the significance of dense ice amount. Because some soft ice (such as snow) and raindrops may slightly reduce the 85 GHz brightness temperature, they may also be interpreted as dense ice by the retrieval algorithm (although the magnitude should be very small). Also, the algorithm itself may produce error in dense ice amount. Therefore, to safeguard the significance of dense ice amount the authors have chosen $f = 0.75$.

The classification scheme was validated by aircraft radar data obtained from the TOGA experiment in the tropics (Liu *et al.*, 1995). In summary, the classification scheme generally works well for most of the clouds in this region, showing good agreement with radar observation for large cloud systems and being able to distinguish reasonably well between precipitating and non-precipitating clouds. However, the classification scheme has difficulties in resolving the small, isolated clouds that are sometimes associated with locally heavy rainfall.

The results obtained by Wang *et al.* (1998b) lead to the conclusion that thick cirrus clouds with large ice particles may be sensed with millimetre-wave radiometry (the 150 and 220 GHz ranges). Over the land, cirrus clouds may give spurious millimetre-wave brightness temperature signatures, caused by skin temperature reductions due to cloud shadowing. According to the Millimetre-wave Imaging Radiometre (MIR) data, the skin temperature effect may be corrected using the 89 GHz channel, resulting in the T_B at 150 and 220 GHz due to ice particle scattering. The thick cirrus, for which the millimetre-wave measurements are useful, has saturated infrared temperatures and attenuated lidar backscattering. Thus, these results illustrate the potential utility of millimetre- and sub-millimetre-wave radiometry for complementing the visible and infrared measurements of cirrus cloud microphysics.

A radically new classification method is developed based on investigation of geometrical multi-fractal features (but not radiance discrimination) of various cloud types (Lovejoy and Mandelbrot, 1985; Lovejoy and Schertzer, 1985; Baryshnikova *et al.*, 1989a, b; Davis *et al.*, 1994, 1996). The geometrical approach is still at a primitive stage of development. But there is no question that the potential integral discrimination schemes using both radiance infrared and microwave variations and fractal geometrical features of cloud systems can give encouraging results.

12.2.2 Microwave remote sensing of rainfalls

A key link in the hydrological cycle is rain that falls from cloud systems in the tropics, which amounts to two-thirds of total global precipitation. Precipitation, by means of its associated latent heat release, is a major energy source driving the hydrological cycle and the large-scale circulation of the atmosphere. The vertical profile of latent heat release greatly influences the structure and speeds of the important wave patterns by which events in the tropics affect the global weather and climate (Simpson, 1988; WMO, 1990a,b; Simpson *et al.*, 1988, 2000; Theon *et al.*, 1992; Webster, 1994; Raschke and Jacob, 1993; Trenberth, 1997; Sharkov, 1998; Stockade *et al.*, 1998; Sorooshian *et al.*, 2000).

One of the most crucial and least-known components of the global hydrological cycle is the precipitation over the tropical oceans, which has never been measured before; the indirect estimates can disagree by as much as 100% or more (Theon *et al.*, 1992). Conventional rainfall measurements are scarce in the tropics. Satellite observation is thus the only effective way to provide continuous monitoring of precipitation events. The need to improve satellite retrieval of rainfall rate/amount has motivated the Tropical Rainfall Measuring Mission (TRMM) (Simpson *et al.*, 1988, 2000; Kummerow *et al.*, 1998, 2000; Takanashi *et al.*, 2000), the Global Precipitation Climatology Project (GPCP) (Arkin and Xie, 1994) and Precipitation Mission (ESA, 1996c). While the monthly time scale has been the focus of most satellite retrieval efforts, it is becoming increasingly apparent that higher space and time resolution rainfall products are needed for diagnostic studies of air/sea interactions and to provide forcing for ocean models.

The current satellite rainfall observations and retrieval algorithms can be categorized into infrared (IR), visible and infrared combined (VIS/IR), passive microwave, and a combination of IR, passive microwave and radar microwave.

Visible/infrared radiation upwelling from clouds, and eventually measured by space-borne radiometers, is reflected/emitted by the top layers of the clouds, and it is (at most) weakly correlated to the microphysical structure of the underlying cloud and precipitation layers. Thus, the VIS/IR precipitation retrieval algorithms cannot be based on information directly associated with precipitation, but are based on the fact that high and thick – i.e. highly reflective and radiometrically cold (for VIS/IR radiation, respectively) – clouds are associated with precipitation, particularly in convective systems.

Two limitations of the VIS/IR optimization method should be emphasized. First, it can be only provide an indication of rain/no-rain, and not a quantitative rainfall rate. Second, it will fail if the region outside the radar coverage has a different type of rainfall from that within the radar coverage. In addition, all that can be said about the adjacent region is the fractional area containing rain. A method of conveying this into the average rainfall rate is needed. Probably, VIS/IR from a geostationary imager would be sufficient.

Passive and active microwave measurements from air/space-based instruments have, in principle, a great potential for estimating precipitation because the upwelling radiation over the precipitating cloud is directly responsive, in a frequency-dependent fashion, to precipitation microphysics. Since the passive microwave precipitation retrieval techniques are linked in a more direct way to the physical characteristics of the rainfall itself than the infrared techniques, more accurate instantaneous rainfall rates can, in principle, be determined using the microwave techniques.

In comparison with visible/infrared observations, passive microwave observations provide better physical information for estimating surface rainfall because microwaves can penetrate clouds and interact directly with hydrometeors at lower levels. The upwelling passive microwave brightness temperatures are determined from the surface emissivity and vertical distributions of the ice and liquid content of clouds. At low microwave frequencies (<37 GHz) the brightness temperature

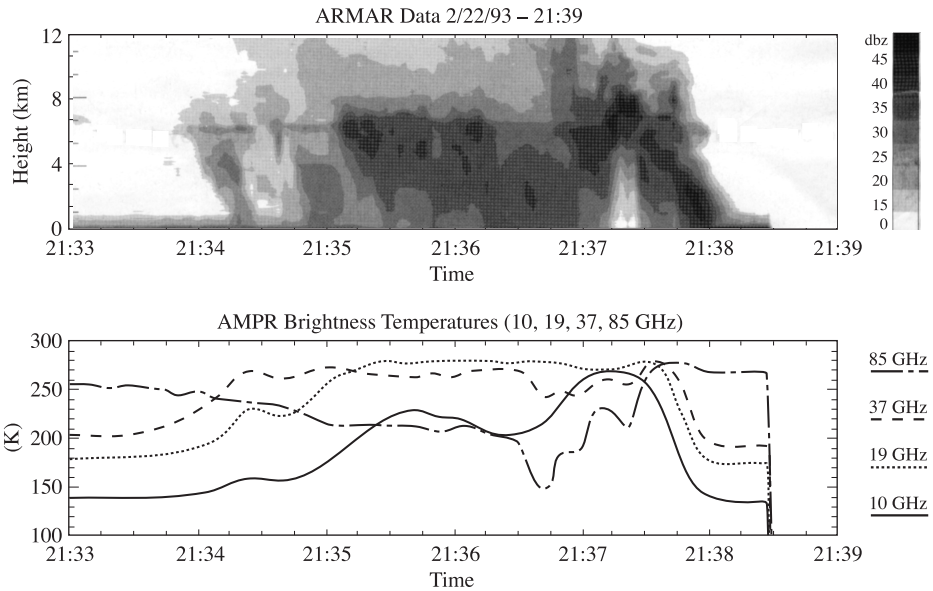

Figure 12.7. Backscattering and thermal radiation signals of a tropical convective cloud system observed by the Airborne Rain-Mapping Radar (ARMAR) and the Advanced Microwave Precipitation Radiometer (AMPR) during TOGA COARE (22 February 1993): (a) radar reflectivity altitude profile of the convective cloud from ARMAR; (b) the spatial profile of brightness temperatures from AMPR for 10, 19, 37 and 85 GHz (Hong *et al.*, 2000).

responds mostly to emission from rain and cloud liquid, and thus the observed brightness temperature increases over the radiometrically cold ocean. In contrast, at high frequencies (>37 GHz), the brightness temperature responds mainly to scattering from cloud ice, and the observed brightness temperature decreases over both ocean and land backgrounds. Figure 12.7 depicts one instructive experimental case that was observed by the Airborne Rain-Mapping Radar (ARMAR), which measured backscattering fields, and the Advanced Microwave Precipitation Radiometre (AMPR), which measured thermal radiation fields, during the Tropical Ocean and Global Atmosphere Coupled Ocean – Atmosphere Response Experiment (TOGA COARE) (Hong *et al.*, 2000).

Rainfall retrieval from satellite and aircraft passive microwave brightness temperatures has been investigated by many researchers using various approaches, from a linear regression (Allison *et al.*, 1974; Wilheit and Chang, 1980) to complicated model-retrieval brightness temperature procedures (Tsang *et al.*, 1977; Viltard *et al.*, 1998; Marzano *et al.*, 1999; Hong *et al.*, 2000).

However, the estimates of precipitation derived from modern satellite microwave observations currently suffer from a serious drawback. Owing to the complexity of the problem and to difficulties related to the characteristics of the radiometers which have been used so far, the quantification of precipitation from satellite passive microwave radiance data still remains, to a large extent, unresolved.

Several algorithms for the retrieval of precipitation have been proposed in the last decade or so, but a consensus algorithm has yet to be developed by the scientific community – for a brief description of several passive microwave algorithms, mostly based on the DMSP-SSM/I (Defence Meteorological Satellite Program – Special Sensor Microwave Imager) image data, and one based on the NOAA-MSU (Microwave Sounding Unit) vertical profile data (see ESA (1996c) and Sharkov (1998)).

The data furnished by SSM/I have been used to provide estimates of precipitation, but suffer from problems, which are due not only to deficiencies of the retrieval techniques themselves, but also to the characteristics of the instrument such as the SSM/Ts space and temporal sampling, which is not adequate for correct observation of precipitation, as well as its frequency selection and scan geometry. The Special Sensor Microwave/lmager (SSM/I) aboard the Defense Meteorological Satellite Program (DMSP) spacecraft provides infrequent sampling, especially in the tropics. Even with the two separate DMSP spacecraft at present in operation, the average local coverage is only about twice a day. The inadequate temporal coverage of SSM/I seriously limits its application in climatic studies. It has been reported that precipitation in the tropics undergoes a preferred diurnal cycle depending on location. Therefore, even with accurate instantaneous precipitation retrieval, the SSM/I observations are not suitable for estimating daily rainfall accumulations because two samples are far from sufficient to capture the daily averaged precipitation.

The detailed analysis of requirements for satellite missions for rainfall measurements and for verification of satellite rainfall algorithms is contained in books (Atlas *et al*., 1984; Ferraro *et al*., 1996; Gairola, 1999; Olsson, 1996; Rodgers *et al*., 1994; Ruf *et al*., 2000; ESA, 1996c; Sharkov, 1998).

12.3 MICROWAVE REMOTE SENSING OF SURFACE OCEANIC HEAT FLUX FIELDS

The ocean interacts with the atmosphere through exchanges of momentum, heat and moisture. The differential heating of the atmosphere by the ocean fuels atmospheric circulation, which, in its turn, drives ocean currents and redistributes the fuel. Short-term climate changes are believed to be strongly influenced by such exchanges. Locally, the ocean absorbs heat in the summer and releases it in the winter; globally, heat accumulated in the tropics is transported poleward by ocean currents. The redistribution of heat reduces the extreme temperature contrasts that otherwise would exist. The heat and moisture fluxes change both the horizontal and the vertical density gradients of the atmosphere and the ocean. They, in their turn, modify the wind and current shears. The moisture flux associates the energy cycle to the hydrological cycle. In the atmosphere, condensation provides not only the means for precipitation, but much of the diabatic heating as well. In the ocean, evapouration cools the upper layer and increases the salinity. The ocean exchanges heat with

the atmosphere through radiative and turbulence processes. Both the sensible heat and moisture fluxes are largely transported by turbulence in the atmosphere. The moisture flux carries latent heat, which is much greater than the sensible heat, both in the mean and the variability over much of the ocean. In the past, large-scale fluxes were computed using meteorological reports from ships of opportunity. In the tropical and southern oceans, ship observations are sparse, so the temporal and spatial variabilities of fluxes cannot be determined accurately using the ship data alone. Space-borne sensors can provide repeated global coverage of meteorological parameteres. So, observations of the sea surface using infrared or microwave radiometers provide important information for studying the dynamical and thermodynamical processes in the upper ocean layer and in the atmospheric layer. Both infrared and microwave radiometers measure the water temperature in a thin layer near the water surface, the so-called skin layer. Its thickness is of the order of a few hundredths of a millimetre for infrared measurements and a few millimetres or smaller for microwave radiation. The processes of heat, moisture, and momentum exchange between the ocean and atmosphere result in water-temperature profiles with very large gradients near the sea surface. For this reason the water temperature, determined with standard *in situ* measurements (at a depth of 1 or 2 m) and with microwave and IR instruments, can be substantially different. The understanding of physical processes that control the temperature profiles near the sea surface is one of the critical points for satellite oceanography (Robinson, 1985; Blume *et al.*, 1977; Liu, 1990). The heat flux in water is dominated by turbulent and molecular transport. However, very close to the surface, in a layer of about 0.5 mm, the turbulent heat transfer at the surface is zero and, hence, at some depth in the range of 0.02–0.5 mm the main contribution to the total heat flux is made by the molecular conductivity of water. If the temperature profile, or at least the temperature gradient, is measured within this layer, it is possible to recover the total heat flux between the ocean surface and atmosphere.

The idea to use the microwave multiwave sensing instruments (passive radiospectroscopy) with different skin depths in the non-isothermal sea surface skin-layer for measuring the water temperature gradient was proposed for the first time by Sharkov (1978). However, in the microwave range the problem of these measurements is complicated, since the surface emission essentially depends on sea-wave conditions, so the wave intensity and wave-breaking can vary in wide ranges. Nevertheless, such or similar approaches can be used well in laboratory practice (Gaikovich *et al.*, 1987), as well as on moving ships (Trokhimovski *et al.*, 1998; Cimini *et al.*, 2003) and on low-altitude airborne platforms.

The modern methods for diagnosis of large-scale thermal interaction between the ocean and the atmosphere from satellite microwave measurements follow the approach based on the semi-empirical equations of a global aerodynamic method (the so-called meteorological bulk parameterization) used as a connecting link between the radiative and heat-exchange characteristics of these environments. A physical foundation of this approach is the fact that the main parameters in the bulk formulas (the ocean surface temperature, air temperature and humidity, wind speed in the near-surface atmosphere) are directly involved in the formation and

transformation of the natural microwave radiance of the ocean–atmosphere system (Liu, 1990).

Another strategy for using the satellite microwave radiometric measurement data is associated with the assimilation of these data in the form of direct indicators of the intensity and the dynamics of heat and moisture exchange (Olson *et al.*, 1999; Grankov *et al.*, 2000). This approach corresponds to the idea of using remote microwave measurement data not only to convert them into parameters accepted in geophysics (temperature, moisture content of the medium, wind speed, etc.), but also to characterize the generalized (essentially thermal energy) indicators, such as the radiation index of the ground surface dryness, the intensity of heat and moisture exchange between the atmosphere and the ground surface, the latent heating distribution and other elements of the energy budget.

As inferred from Chapter 10, the measurements of upwelling microwave brightness temperatures provided by microwave instruments are sensitive to observed distributions of precipitating liquid and ice-phase hydrometeors. Since precipitation is the end-product of hydrometeor phase-change processes in clouds, and since the latent heat is released and consumed by these processes, the passive microwave measurements yield an indirect measurement of latent heating processes. A method for remote sensing of three-dimensional latent heating distributions in precipitating tropical weather systems from the satellite passive microwave observations was developed by Olson *et al.* (1999). In this approach, the cloud model that simulated hydrometeor latent heating vertical profiles, which have radiative characteristics consistent with the given set of multispectral microwave radiometric observations, was composed to create the best estimate of the observed profile by the special retrieval 'Bayesian' technique. An estimate of the areal coverage of convective precipitation within the radiometer footprint is used as an additional constraint on the contributing model profiles. This constraint leads to more definitive retrieved profiles of precipitation and latent heating in synthetic data tests. The remote sensing method is applied to Special Sensor Microwave/Imager (SSM/I) observations of tropical systems, which occurred during the TOGA COARE, and to Hurricane Andrew observations (1992). Although the instantaneous estimates of rain rates are high-biased with respect to coincident radar rain estimates, the precipitation patterns are reasonably correlated with radar patterns, and the composite rain rate and latent heating profiles show respectable agreement with estimates obtained from forecasting models and from heat/moisture budget calculations (Rodgers and Adler, 1981; McMurdie and Katsaros, 1985; Rodgers *et al.*, 1994; Sharkov, 1998; Nerushev *et al.*, 2001).

Another approach was developed by Grankov *et al.* (2000). Based on the results obtained in the Atlanteks-90 experiment and simulations, it has been shown that the brightness temperature of the ocean–atmosphere system's microwave emission can serve as a direct numerical characterization of synoptic variations in the intensity of heat and moisture exchange at its interface. The parameters interlinking heat fluxes and the ocean–atmosphere system brightness temperature are the emission of molecular oxygen in the resonance band at 5 mm, and the total atmospheric moisture content in the 1.35-cm resonance line. The interrelation, for example,

between the mean daily variations of fluxes of total (latent and explicit) heat and the ocean–atmosphere system's brightness temperature, is very close; the value of the correlation coefficient between these quantities varies from 0.83 to 0.92 as a function of the radiation wavelength; the brightness temperature reacts particularly clearly to the sharp changes in heat fluxes observed in the Atlanteks-90 experiment in the period of cyclonic reconstruction of the atmosphere. The results of this analysis confirm the role of the total atmospheric moisture content in the processes of heat and moisture exchange at the ocean – atmosphere system's boundary, divide on synoptic time scales and, at the same time, attest to the importance of this parameter as a remote characteristic of the thermal state of the system.

Below we shall consider in more detail the radiothermal methodology of studying the transition skin-layer of the ocean–atmosphere system.

12.3.1 Radiothermal spectroscopy of the ocean–atmosphere transition layer

As we have noted, an important example of non-isothermal structure in the ocean – atmosphere system is the transition microlayer on the ocean surface through which the mass- and heat-transfer between the ocean and atmosphere occurs. The problem of studying the heat exchange between the ocean surface and the atmosphere within the framework of the small-scale interaction model is reduced (under weak sea wave conditions) to the problem of experimental determination of characteristics of temperature profile characteristics in the thin stable surface layer of the sea.

The use of unique contact instruments made it possible to find, that the temperature profile in the surface layer of the sea, which exists both at night and in the day, is highly non-isothermal and has an exponential character (Khundzhia *et al.*, 1977; Robinson, 1985):

$$T(z) = T_2 + (T_1 - T_2)\exp(-\beta z). \tag{12.8}$$

where $T(z)$, T_1 and T_2 are temperatures, respectively, at depth z, at the depth of isothermal layer bedding and on the surface. Such a 'cold' surface layer 2–5 mm to 10–20 cm deep was recorded, for example, in the Black Sea (in summer and autumn) with sea waves up to wind force 3 (Khundzhia *et al.*, 1977). In the same paper it was shown that the value of the total heat energy flux (q) from the sea to the atmosphere, which is composed of molecular heat exchange on the ocean–atmosphere boundary, and of latent heat for water evapouration from the sea surface, is determined by the following expression:

$$|q| = \Lambda\beta(T_1 - T_2), \tag{12.9}$$

where Λ is the molecular heat conduction coefficient of ocean water. Thus, from experimentally found characteristics of the temperature profile (the difference between T_2 and T_1 and quantity β) one can determine the total heat flux returned by the sea into the atmosphere during thermal interaction. The determination of features of the spatial structure of the temperature field of the sea's subsurface layer by the remote sensing method can have a defining significance in heat- and mass-exchange processes in the open sea. However, the use of IR thermal systems for

solving the mentioned problem is inconvenient, since the effective emitting layer in this band of electromagnetic waves represents a very thin surface film having a thickness of the order of 5–10 micrometre, and for this reason the contribution of the considered non-isothermal character of temperature to the IR thermal radiation is low.

A more optimal remote sensing technique, which allows one to approach the experimental solution of the problem of determining small-scale heat exchange characteristics at the ocean–atmosphere boundary, is the use of radiothermal microwave instruments (Sharkov, 1978), because the effective emitting layer in this band extends up to a thickness compared with the 'cooled' transition layer, and the contribution of the non-isothermal character of temperature to the radio-emission of such a surface will be considerable.

In this problem it is possible to use the approximation of radiation of non-uniformly heated absorbing medium with allowance for refractive distortion of a flux (see relations (7.101) and (7.102)). Using these relations, after some transformations we shall obtain the following expression for the contrast of radiobrightness temperature ΔT_B of a quiet water surface with temperature T_2, caused by the non-isothermal character of the subsurface layer:

$$\Delta T_B = \kappa(\lambda, \theta, T) \frac{T_1 - T_2}{1 + \dfrac{\beta}{\gamma(\lambda) S(\theta, \lambda)}}, \tag{12.10}$$

where $\gamma(\lambda)$ is the coefficient of attenuation in the sea medium, λ is the working wavelength. Figure 12.8 presents the spectral dependencies of the $\Delta T_B / \Delta T_0$ ratio, where $\Delta T_0 = T_1 - T_2$ at nadir-looking observation for a fresh (salinity of 0‰) and

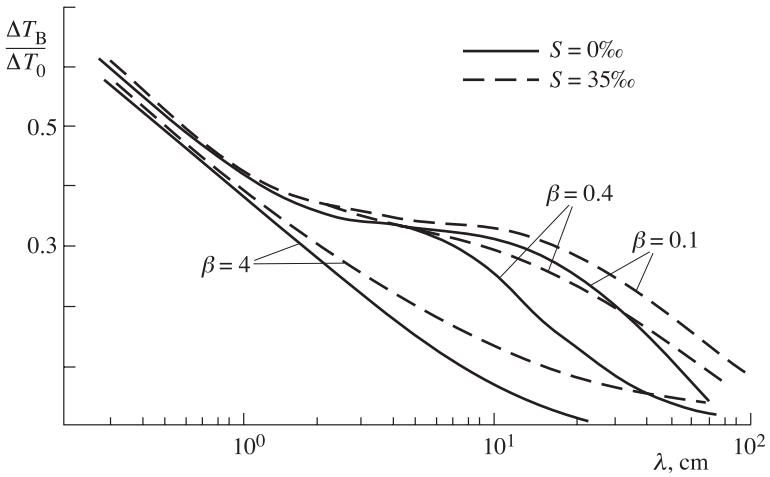

Figure 12.8. Theoretical microwave spectra of relative variations of the brightness temperature for water surfaces with a non-isothermal skin-layer in a nadir sensing of fresh ($S = 0‰$) and sea ($S = 35‰$) water and for the following profile parameters: $\beta = 0.1, 0.4, 4.0$.

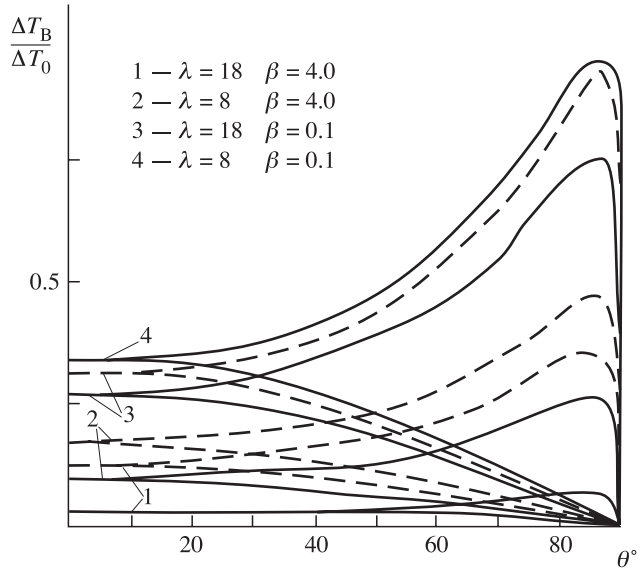

Figure 12.9. Polarization characteristics of relative variations of the brightness temperature for water surfaces with a non-isothermal skin-layer in a nadir sensing of fresh (solid curves) and sea (dashed curves) water and for the following profile parameters: $\beta = 0.1$ and 4.0, and at wavelengths 8 and 18 cm.

ocean water (salinity of 35‰), as well as for three temperature profiles (β values of 0.1, 0.4, 4.0 cm^{-1}). The former values of β correspond to shallower sections of water areas; the last value corresponds to deeper ones. The analysis of Figure 12.8 indicates that the most informative, from the viewpoint of recognition of the profile gradient (quantity β) for fresh and for sea water is the long-wavelength portion of the centimetre and the short-wavelength portion of the decimetre wavelength band. Radio-emission in the band of wavelengths shorter than 1 cm is formed by a thin water interlayer, and, by virtue of this fact, the addition to radiobrightness temperature is mainly caused by the surface temperature variation. In the long-wavelength portion of the decimetre wavelength band (longer than 50 cm) the effective layer of radio-emission both for sea and for fresh water essentially exceeds the non-isothermal region, and the contribution of this temperature profile feature into radio-emission decreases. The analysis of polarization characteristics of the relative addition to radiobrightness temperature, caused by the non-isothermal character of the temperature profile (Figure 12.9) indicates, that the $\Delta T_B/\Delta T_0$ dependence is qualitatively similar to the polarization characteristics of a smooth water surface – there is a prominent Brewster angle for the vertically polarized radiation component.

To solve the reverse problem, that is, to derive the $\Delta T_0 = T_1 - T_2$ difference and parameter β from the results of radio-emission measurements at several wavelengths, it is possible to make use of the construction of nomograms, which have the form of a set of intersecting straight lines in the problem under consideration. Figure 12.10

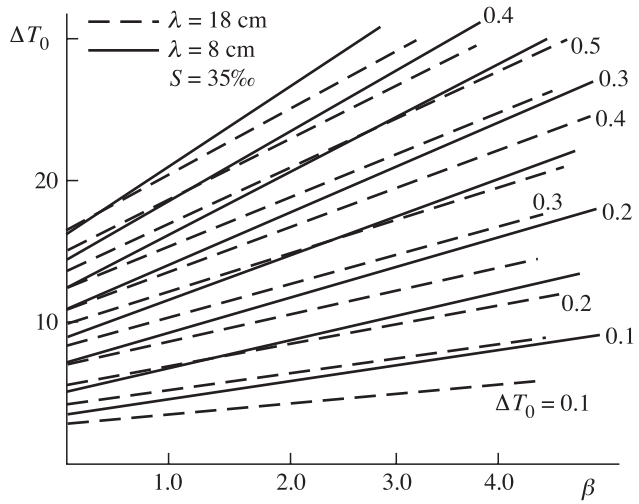

Figure 12.10. Diagram for recovering profile parameters ΔT_0 and β for sea water surface using measurements at two wavelengths, 8 and 18 cm. The measured parameter ΔT_B varies from 0.1 K in intervals.

presents the nomograms in ΔT_0–β coordinates, calculated by (12.10) for two wavelengths, 18 and 8 cm, and for sea water of salinity 35‰. The parameter of sets is presented by the values of contrasts of radiobrightness temperatures obtained at observation of regions with various degrees of the non-isothermal property. The use of a component with an observation angle near the Brewster angle for reception of radio-emission of a vertically polarized component can increase by a factor of 2–2.5 the absolute measured values of contrasts of radiobrightness temperatures.

Since in actual observed cases ΔT_0 varied from 0.1 to 3°C, then, as follows from Figure 12.8, the contrast to radiobrightness temperature will constitute rather small values – degrees and fractions of a degree. The techniques close to this procedure have been successfully applied under laboratory conditions (Gaikovich *et al.*, 1987) and on board the research ship (Trokhimovski *et al.*, 1998). The now available high-sensitive multi-frequency radiothermal onboard complexes allow one to hope for a successful experimental solution of the important problem of ocean – atmosphere heat exchange under consideration.

12.4 MICROWAVE REMOTE SENSING OF THE OCEANIC SURFACE

As we have already noted, the inclusion of methods and means of microwave diagnostics into space observations in the period 1968–1979 (on the 'Cosmos-243', 'Cosmos-384', Seasat, and Nimbus-7 satellites) was undoubtedly a principal stage in the development of remote sensing of the World Ocean. The study and understanding of microwave patterns of the ocean surface have provided a significantly different

(as compared to the case of using the optical and infrared bands only) physical information capacity of microwave sensing in studying such dynamical objects as disturbance of the sea surface. This relates, first of all, to spatial–temporal statistical features of the sea state and the surface wind field. The electrodynamic properties of the sea surface disturbance and, first of all, the intensity of microwave radiation, is determined by the two areas of physical phenomena. The first one is related to the degree of roughness of the ruffled (but continuous) surface, or, in other words, with spatial features of the sea disturbance spectrum considered as a spatial–temporal statistical object (see Chapter 2). The second area is related to disturbatance of the sea medium continuity, which reveals itself as breaking sea waves and the appearance of the intensive drop-spray phase and the bubble disperse phase of sea foam. Here, again, the consideration is performed within the framework of studying the electrodynamic properties of disperse media (see Chapter 10). The mentioned subdivision, certainly, is rather conventional, since the spatial-phase transformations belong to the same physical object. Nevertheless, from the viewpoint of electrodynamic models research, as detailed investigations have shown, such a subdivision is, undoubtedly valid. Each of these approaches has till now taken an individual direction of investigations, both in the experimental and the theoretical respect. Below we shall briefly consider some historical aspects and the modern state of investigations in these areas.

12.4.1 Rough sea surface

The results of theoretical investigations (Stogryn, 1967; Shulgina, 1972; Martsinkevich and Melentyev, 1975; Wentz, 1975; Wu and Fung, 1972) of the thermal radiation of a rough surface within the framework of geometrical optics approximation and using the statistical data on sea surface slope distribution of gravitational waves (Cox and Munk, 1954; Martsinkevich, 1970) gave rise to the statement of detailed experimental investigations, which were carried out in 1969–1970 from the special platform of the Argus Island tower near Bermuda at rough sea conditions (Hollinger, 1971). The experiment has demonstrated a fairly high sensitivity of brightness temperature variations on the horizontal polarization at 40–70° incidence angles to the wind speed under variable disturbance conditions and made it possible to obtain for the first time numerical values of gradients in the dependence of radiation intensity on the surface wind speed. Note that the wind speed magnitude only is meant here.

It was the results of these experiments that later underlay the measurement ideology and data processing algorithms for the Scanning Multichannel Microwave Radiometre (SMMR) installed on board the Seasat spacecraft (July–October 1978) and the Nimbus-7 satellite (launched in 1978). Using linear regression models, the global map of speeds (the speed magnitude) of the surface wind in the World Ocean area was first reconstructed for a period of one month (Prabhakara *et al.*, 1983). A series of interesting experiments (for example, by Kondratyev *et al.*, 1975; Martsinkevich, 1981; Guissard and Sobieski, 1987; Wentz *et al.*, 1986; Wilheit *et al.*, 1984; Wilheit and Chang, 1980; Sasaki *et al.*, 1987) were performed later;

however, the question on azimuthal properties of microwave radiation, i.e. on the relationship between the wind speed vector (or the wave vector of an energy-carrying wave) and the vector of linear polarization of the antenna system was not stated.

The experimental detection of stable azimuthal properties of thermal radiation of the disturbed sea surface under full-scale conditions in 1976 marked a radically new stage in the remote sensing of a rough dynamic surface (Bespalova *et al.*, 1979, 1982). This is related, first, to the fact that the obvious azimuthal properties indicate the diffraction character of electromagnetic field interaction with the surface roughness. This fact should be expected, strictly speaking, from general physical considerations, i.e. from the relation between the electromagnetic radiation wavelength and the gravitation-capillary wavelength of sea surface waves. But, because any reliable full-scale data on spatial spectra of gravitation-capillary waves were absent to the time of performing flight experiments, the strong and stable azimuthal effect in the field of thermal radiation of a wave-driven water surface in quite various areas (the open ocean, large lakes) and under various acceleration conditions (developed disturbance, non-developed fetch) was completely unexpected for the researchers. Secondly, the presence of a stable azimuth effect, recorded by remote sensing, makes it possible to restore not only the magnitude, but also the vector of the surface wind, which is an important parameter in the dynamical interaction of a wind flux with the dynamical surface.

The first cycle of airborne measurements of the azimuthal dependence of sea surface thermal emission at different polarizations under various weather conditions were performed by the specialists of the Space Research Institute (Moscow) using airborne microwave instruments with linear polarization during circular flights in 1976–1997 in the high-latitude sea areas of the Barents Sea and the White Sea (Bespalova *et al.*, 1979). The next cycles of these flight experiments were conducted in the Sea of Okhotsk, the Caspian Sea, the Black Sea, the Sea of Japan and Lake Ladoga in 1977–1979 (Bespalova *et al.*, 1982) and then near the Kamchatka peninsula in the north-west Pacific in 1981–1982. The measurements were carried out both far from the shore, where the ocean depth was about 1–5 km, and in the near-shore areas. The wind speed (sea state) and the energy wave fronts were estimated during the first cycle both, visually – by skilled aircraft operators using the Beaufort sea notation – and by processing the aerial photographs. Then the wind speed for these studies was estimated at typical flight altitudes of 200–1000 m using Doppler-based wind drift estimates. From these data the wind speed at the standard altitude of 10 m was calculated using the logarithmic dependence for the wind profile.

While the research aircraft performed circle patterns over wave-driven seas, the microwave radiometers aboard recorded cosine-like variations in brightness. Typical brightness temperature variations, measured during circular flights over the Caspian Sea and the Sea of Japan, are shown in Figures 12.11 and 12.12. The first cycle of measurements were carried out using nadir-looking microwave instruments at wavelengths from 0.8 to 18 cm and the SC-3 scatterometre at the wavelength of 3 cm. Owing to aircraft roll of 5–10° all radiometers were pointed during the circling at the same incidence angle, so that the linear polarizations oriented along the aircraft axis

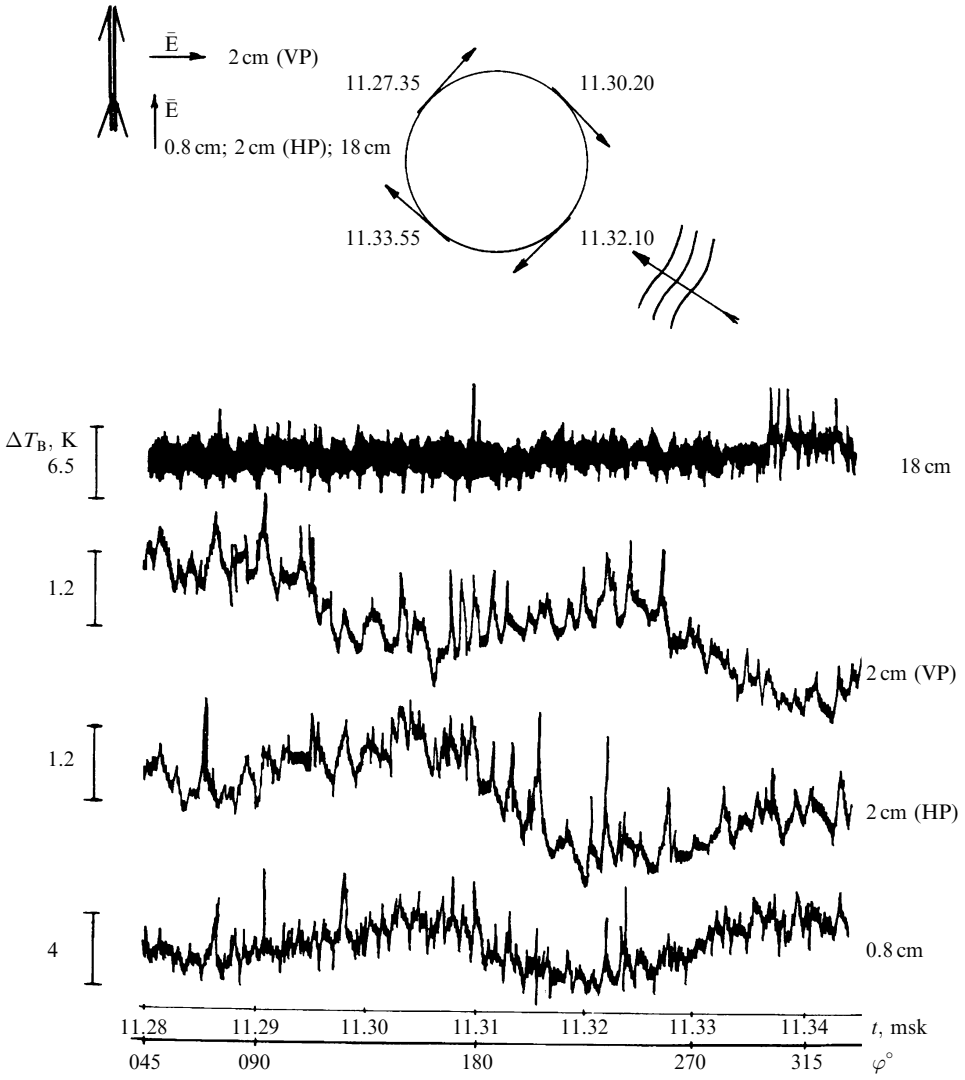

Figure 12.11. The experimental results of flight investigations that made possible the detection of the azimuthal anisotropy effect in sea surface microwave emission. The scheme of circular flights and the positions of the antennas' linear polarization vectors and of surface gravity wavefronts are presented at the top of the figure. The double arrow points along the longitudinal centreline of the research aircraft. The fragments of the output signals of airborne (Russian airplane-laboratory IL-18) radiometer R-18 (wavelength 18 cm), radiometer R2 (wavelength 2 cm, two polarizations: HP, the horizontal polarization; VP, the vertical polarization), and radiometer R0.8 (wavelength 0.8 cm) when circular flights were performed at a height of 300 m and microwave observations were performed with the nadir view angle. The working area is the North Caspian Sea (Russia). The date was 28 November 1977. Moscow time and the brightness temperature intensity scale are shown on the abscissa and on the ordinate.

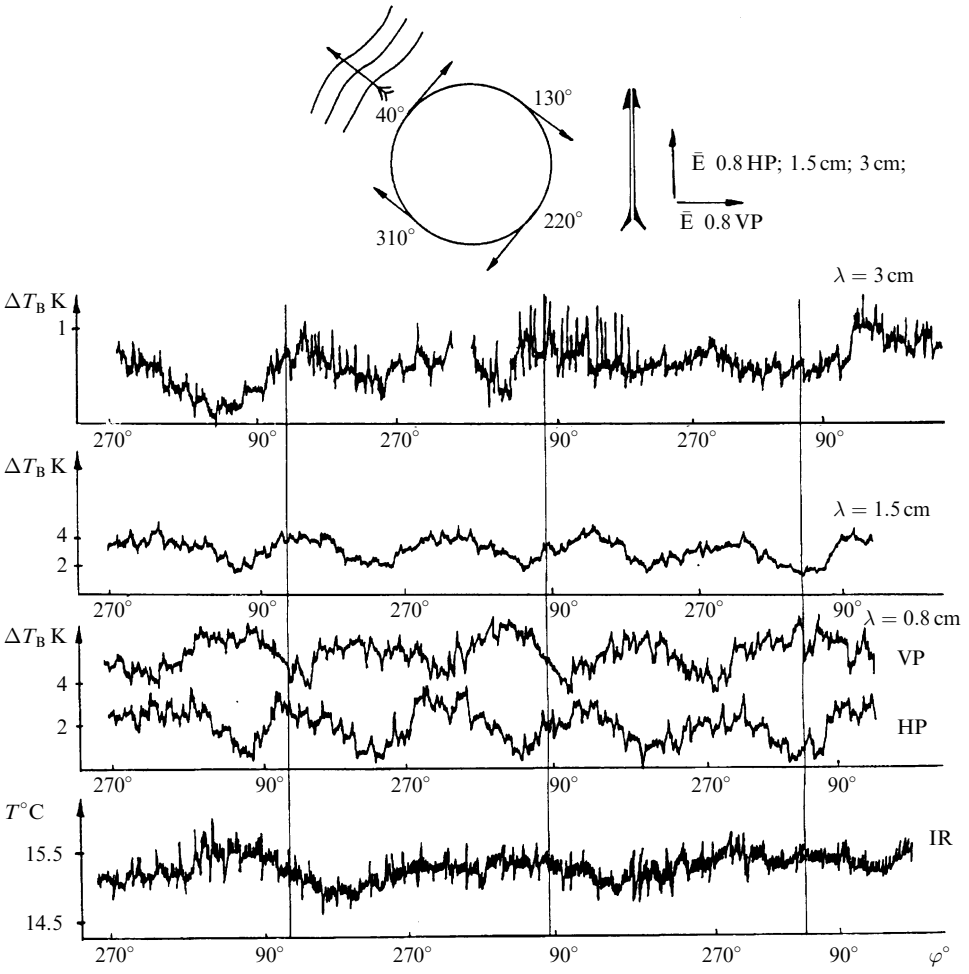

Figure 12.12. The experimental results of flight investigations (10 October 1978, the Sea of Japan) in the azimuthal anisotropy study of sea surface microwave emission. The scheme of circular flights and the position of the antennas' linear polarization vectors and of surface gravity wavefronts are presented at the top of the figure. The double arrow points along the longitudinal centreline of the research aircraft. The fragments of the output signals of airborne (Russian airplane-laboratory IL-14-I) radiometer R-3 (wavelength 3 cm), radiometer R0.8 (wavelength 0.8 cm, two polarizations: HP, the horizontal polarization; VP, the verical polarization), radiometer R1.5 (wavelength 1.5 cm) and IR radiometer when circular flights were performed at a height of 300 m and microwave observations were performed with the nadir view angle. Sea state was 4 on the Beaufort scale. Moscow time and the brightness temperature intensity scale are shown on the abscissa and on the ordinate.

corresponded to horizontal polarization, and the perpendicular polarizations corresponded to vertical one. It is evident that the vertically polarized brightness temperature reaches a maximum in the upwind direction, whereas the orthogonal (horizontal) polarization exhibits a minimum in this same direction. In Figure 12.13 the backscattered signal measured at a view angle of 10° and wavelength of 3 cm is plotted. The azimuthal variations of emitted and backscattered microwave signals were observed to be very similar, thus confirming the hypothesis of a wind-driven wave origin.

The surprising results from the processing of the data of the first stage (1976–1977) of flight experiments, which were obtained under the guidance of the author of this book, have served as a powerful stimulus to the statement of laboratory and theoretical investigations, which were soon performed (Etkin *et al*., 1978; Kravtsov *et al*., 1978). The results of these works served as a basis of a new phase of detailed radiospectroscopic investigations of the emission fields of a wave-driven sea surface (Irisov *et al*., 1987; Yueh *et al*., 1995, 1999; Kuzmin and Pospelov, 1999; Kuzmin *et al*., 2000; Trokhimovskii *et al*., 2000; Kunkee and Gasiewski, 1997; Reising and Camps, 2000; Laursen *et al*., 2000; Stogryn *et al*., 1994; Connor and Chang, 2000; Goodberlet *et al*., 1989).

As frequently happens in the history of the development of science, the effect of azimuthal anisotropy in the field of thermal radiation of the sea surface was, essentially, rediscovered much later (Yueh *et al*., 1995, 1999). Now much attention is given to the detailed study of the features of the field of radiation from the side of both the experimenters and the theorists (Irisov, 1997; Cherny and Raizer, 1998). So, Trokhimovski *et al*. (2000) by rather fine experiments have demonstrated a high sensitivity of the azimuthal anisotropy of thermal radiation of the sea surface to the parameters of the gravitation-capillary part of the sea disturbance spectrum. Trokhimovskii (1997) has demonstrated the possibility of restoring the gravitation-capillary part of the sea disturbance spectrum from the data of the measurement of polarization characteristics of thermal radiation of a wave-driven sea surface.

12.4.2 Sea wave breaking fields

The second complex of physical reasons stipulating a serious contribution to the thermal radiation of a wave-driven sea surface are the processes of the breaking of sea waves and the appearance of an intensive drop-spray phase and a bubble disperse phase of sea foam with their subsequent rapid and complicated spatial–temporal evolution. It should be mentioned that the experimental detection of intensive (of black-body type, virtually) thermal radiation of foam systems by Williams (1969) under very complicated (and, we might add hazardous) hydrometeorological conditions (such as the flight of a sporting-type airplane through the 'wall' of a tropical cyclone) was also rather unexpected for the researchers. This was associated with a supposition on the absence of noticeable absorption and scattering of electromagnetic waves of the microwave band on a set of quite small hollow air spheres and hollow hexagonal structures with very thin films of water that represented the foam system alone (Raizer *et al*., 1976; Weaire and Hutzler, 2000).

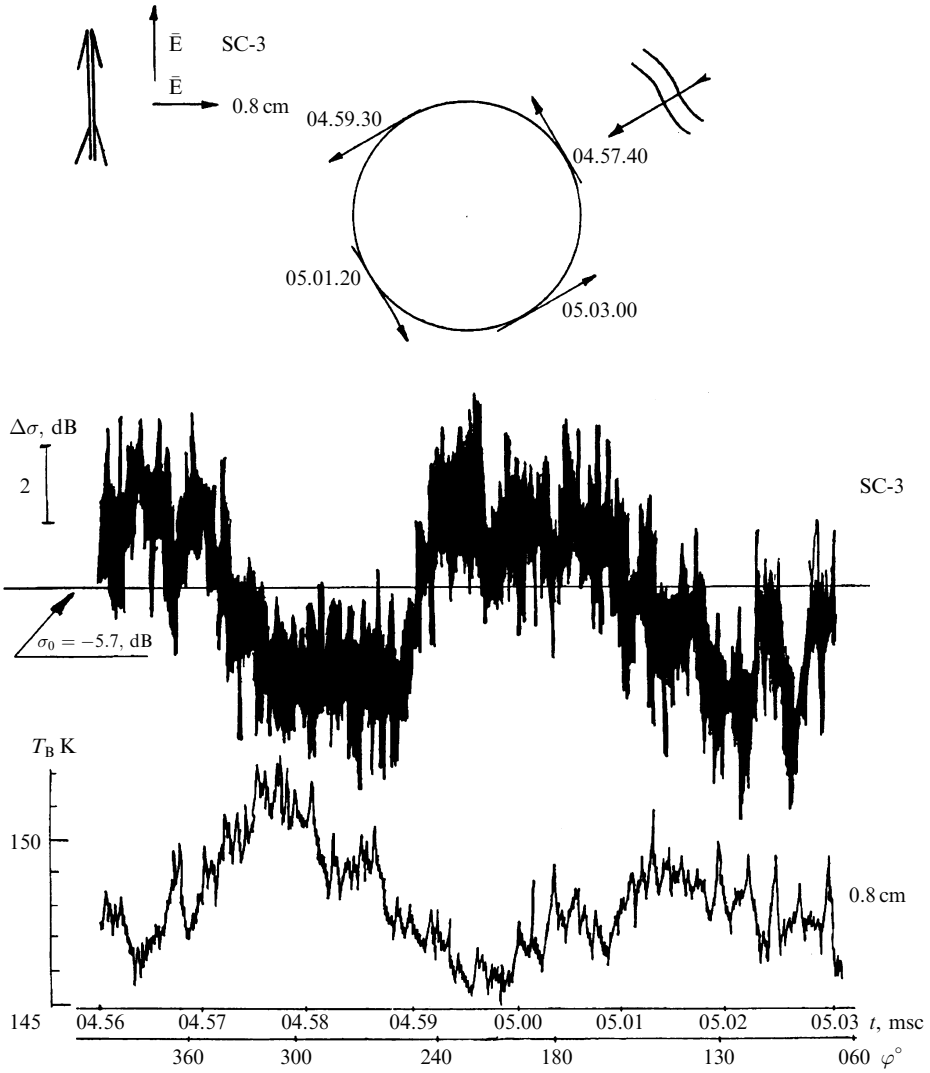

Figure 12.13. The experimental results of flight investigations (20 October 1978, the Sea of Japan) for the azimuthal anisotropy study in sea surface microwave emission and backscattering. The scheme of circular flights and the positions of the antennas' linear polarization vectors and of surface gravity wavefronts are presented at the top of the figure. The fragments of the output signals of airborne (Russian airplane-laboratory IL-14-II) radiometer R0.8 (wavelength 0.8 cm) and of scatterometer SC-3 (wavelength 3 cm) when circular flights were performed at a height of 300 m with the angle of 5° slope and microwave observations were performed with the nadir view angle relative to the aircraft. Sea state was 6 on the Beaufort scale. Moscow time and the brightness temperature and backscattering intensity scales are shown on the abscissa and on the ordinate.

Nevertheless, these results gave rise to the first (and rather naive, as it was found later) ideas and determinate models, according to which the basic elements, which determine the thermal radiation of the wave-driven sea surface, will be the foam systems of various classes and, accordingly, with increasing wind speed (from 5–6 m/s to typhoon velocities of 33–35 m/s) according to the power law (linear or quadratic) the radiation intensity will also increase up to values corresponding to black-body radiation (Droppleman, 1970; Williams, 1971; Matveev, 1971). Further detailed investigations of the radiophysical properties of foam systems and spatial–temporal disperse characteristics of foam systems under full-scale conditions, carried out under the guidance of the author of this book (Militskii *et al*., 1976, 1977, 1978; Bordonskii *et al*., 1978; Raizer and Sharkov, 1980, 1981; Vorsin *et al*., 1984; Bondur and Sharkov, 1982, 1990; Pokrovskaya and Sharkov, 1986, 1987a, b; 1994; Zaslavskii and Sharkov, 1987; Sharkov, 1993a,b, 1994, 1995), have clarified the situation in many respects and indicated the imperfection of primary models and ideas. Below we shall present a brief review of works in this field.

The problem of detecting the effects of radio-emission of a drop-spray zone in sensing the sea surface from a low-flight carrier – an aircraft – has some principal features. In essence, the question is about solitary (in antenna's field of view) and quite non-stationary physical objects possessing high emissivity. This imposes certain requirements on the parameters of onboard instruments, as well as on the choice for conditions for the experiment. So, the value of a radiothermal signal, recorded by a microwave complex installed on a moving carrier, can be presented as follows (see Chapter 5):

$$T_{\mathrm{B}}(t) = \int_0^{\infty} \mathrm{d}\left(\frac{x}{V}\right) h\left(t - \frac{x}{V}\right) \left[\iint G_0(x - x'; y - y') T_{\mathrm{BF}}(x', y', t)\, \mathrm{d}x',\, \mathrm{d}y'\right], \quad (12.11)$$

where $h(t)$ is the impulse response of a receiving device (with the time constant t_0); $G(x, y)$ is the instantaneous field of view of the antenna directional pattern (ADP) on the surface; $(4/\pi)G^{1/2} = 2H \operatorname{tg}(\theta/2)$; H, V are the flight altitude and carrier velocity; θ is the angular resolution of ADP; $T_{\mathrm{BF}}(x, y)$ is the radiothermal image of a foam structure (with the geometric size Δx and area S). This relation implies a great diversity of types of radiothermal signal recorded from a non-stationary, but 'bright' (in the radiothermal sense) object. So, it can easily be seen that for $\tau_0 \ll (\Delta x/V)$ and $G \simeq S_0$ the form of a recorded signal will represent an isosceles triangle with the base $2\Delta x/V$ and height $T_{\mathrm{BF}} - T_{\mathrm{BS}}$, where T_{BS} is the brightness temperature of thermal 'background' of the sea surface (see Chapter 5). As τ_0 increases up to values of $\Delta x/V$, the signal amplitude decreases, though 'the appearance' of a signal does not change qualitatively. If, however, $\tau_0 < (\Delta x/V)$, but $G < S$, then the signal shape represents a 'little house with a cap', and the brightness contrast ΔT_{B} will be the same quantity $(T_{\mathrm{BF}} - T_{\mathrm{BS}})$. If the object has a form of a point source, i.e. $G \gg S$, then the brightness contrast will have the other value $\Delta T_{\mathrm{B}} = (S_0/G)(T_{\mathrm{BF}} - T_{\mathrm{BS}})$, and the signal shape 'appearance' will describe the shape of a main lobe of the antenna directional pattern (see the characteristic example in Chapter 5).

The representative implementation of a radiothermal signal from the wave-

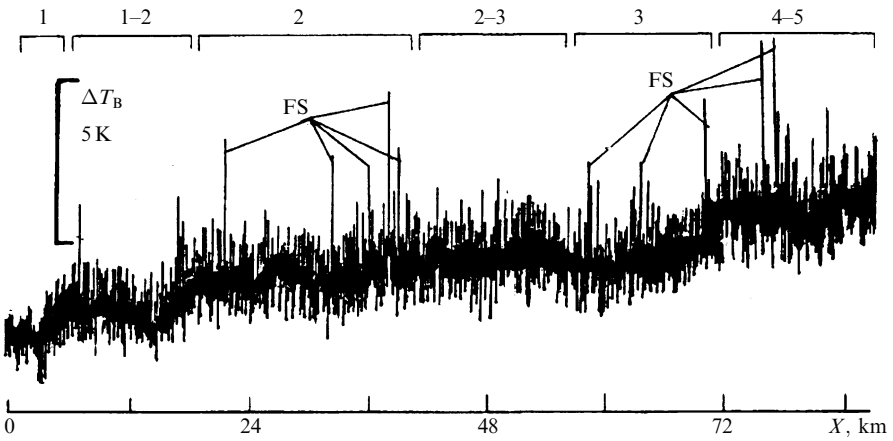

Figure 12.14. Fragment of the output signal of airborne (Russian airplane-laboratory IL-18) high-performance radiometer R2 (wavelength 2 cm) versus the flight distance X (km). The linear flight was performed at a height of 1000 m with the nadir view angle relative to the aircraft as the sea state increased from 1 ball to 5 balls in Beaufort notation. The working area is the north Caspian Sea (Russia). The date was 27 November 1977. FS are the emission signals from foam structures. Figures show the Beaufort numbers for the sea state.

driven sea surface (Figure 12.14) was obtained under the following conditions: the Caspian sea water area, a direct track extending 80 km along the section with seaway variation from 1 to 4 points of the Beaufort notation (according to visual estimates of a skilled on-board meteorologist); flight altitude $H = 1000$ m, carrier velocity $V = 350$ km/hour. The instruments consisted of a high-sensitivity radiometric system of the 2-cm band, with a sensitivity threshold of about $\Delta T = 0.03$ K with time constant $\tau_0 = 1$ s, and was installed aboard the Il-18 laboratory aircraft with a mirror-reflecting parabolic antenna with the directivity pattern width $\theta = 1.5°$. The resolution spot on the surface for nadir-looking observation was $G = 25$ m. The analysis of Figure 12.14 indicates that, along with general increase of brightness temperature with seaway amplification caused by small-scale seaway components (including the azimuthal anisotropy effect), the presence of acute spikes – the signals from the foam-disperse zone – is characteristic. The synchronous air photography gave an idea of the sea surface structure under 4-point seaway conditions: the size of foam formations, generated at wind wave breaking, were of the order of 3–10 m. By virtue of a small time constant of integration $\tau_0 = 0.05$ s (in the flight mode), the amplitudes of ejecta were recorded virtually completely, the radiothermal contrasts being equal to 3–4 K. The experimental situation corresponds to the condition of $G > S_0$, and, thus, $(T_{BF} - T_{BS})$ will be 80–100 K, which fully corresponds to theoretical estimations (Raizer and Sharkov, 1981). The second interesting example represents synchronous registograms of a scatterometre (3 cm) and radiometers (2 cm and 8 mm) obtained under 5- and 6-point seaway conditions

in performing circular flights (at an altitude of 300–600 m). They are presented in Figures 12.11 and 12.13. The registograms of microwave instruments clearly exhibit the signals from foam structures having the form of 'triangles' with contrast amplitude of the order of $T = 2$–4 K. Since the experimental situation is such, that $G > S_0$, but in this case $\tau_0 > \Delta x/V$, the low values of radiothermal contrasts are clear. Of importance is the fact that the scatterometre channel does not indicate the presence of foam structures because of their small reflectivity (Militskii *et al.*, 1976, 1977). However, subsequent full-scale investigations have shown (Cherny and Sharkov, 1988) that, in general, the situation is more complicated, and the relationship between the values of radiation and backscattered signals depends on the temporal stage of wave-breaking and on the appearance of a drop-spray phase against the background of foam structures, the drop-spray phase making a noticeable contribution to the backscattered signal. As the seaway amplifies (the sea surface state (SSS) is more than 6 points in the Beaufort notation), the regular azimuthal dependence (Figures 12.11 and 12.13) of polarization anisotropy is violated: the radiothermal field acquires more isotropic character, since a noticeable contribution to radio-emission is made by the drop-spray phase and foam formations, the obtaining of which does not have any azimuthal features regarding the wind direction.

Thus, in aircraft sensing the contribution of foam structures to the sea surface radiation can give signals of a diverse character, and the thermal radiation of individual foam structures can be revealed only by using synchronous air photography at high spatial resolution (10–20 cm), which is, obviously, not always possible. On the other hand, the use of a less high-speed and more manoeuvrable carrier – a helicopter – will allow for essentially increasing the observation time that considerably facilitates the experimental problem. In this case it is possible to perform detailed air photography of the studied surface for further identification of the data (Bondur and Sharkov, 1982, 1990).

In observation from space carriers, where the linear size of the field of view of the radiothermal instruments' antenna equals 10–50 km, the recorded signal quantity can be written as:

$$T_{\mathrm{B}} = T_{\mathrm{BS}}\left(1 - \sum_{i=1}^{N(t)} S_{\mathrm{F}i}\right) + \sum_{i=1}^{N(t)} T_{\mathrm{BF}i} S_{\mathrm{F}i}, \tag{12.12}$$

where $N(t)$ is the number of foam structures in a frame corresponding to a displayed 'spot' of the antenna directional pattern (ADP) on the surface. In this case it is necessary to know the detailed statistics of spatial fluctuations $N(t)$ in the appropriate spatial frame, as well as of geometric and emissive characteristics of foam systems of various types and the time of their 'life'. These issues have been thoroughly studied in a cycle of works (Pokrovskaya and Sharkov, 1986, 1987a,b, 1994; Srokosz 1986; Zaslavskii and Sharkov, 1987; Bondur and Sharkov, 1982, 1990; Sharkov, 1993a,b, 1994, 1995). So detailed experimental results have shown (Pokrovskaya and Sharkov, 1987a,b, 1994; Sharkov, 1993a,b) that the stochastic model of large-scale breaking wave fields may be presented as a stochastic spatial whole-

numbers field of Markov type (the Poisson process) with independent discrete sources (events). The mean value of the specific density of foam structures (the centres of wave energy scattering) has a clear, strong (cubic) tendency to increasing with the wind speed and has a 'threshold' nature (the stepwise approximation) at a wind speed of 5 m/s (Bondur and Sharkov, 1982). It is interesting to note that later this relationship has also been found theoretically by Phillips (Phillips, 1988).

Detailed experimental investigations of the process of breaking and subsequent decaying of foam systems (Sharkov, 1994, 1995; Sharkov, 1996d) have shown that the process of gravity wave 'preparation' to breaking fall and the breaking itself takes some fraction (about 1/3) of the wave period. In other words, the nonlinear stage of the breaking process and the formation of a wave crest foam grows at fabulous rates. However, the process of decay of patch foam structures of a foam mass is characterized by exponential decay with considerable half-decay time (0.5–10 s), which depends on the physicochemical properties of sea water in the area.

Some new specific group of wave breakings, called microbreakings (MB), was detected by Sharkov (1994, 1995). MB have some particular properties: a short lifetime of the foam mass ($\sim$1 s); a small characteristic size ($\sim$0.4 m); the absence of accompanying patch foam; the faint optical contrast; wave–wind conditions being independent of average size. The instantaneous value of the surface foam covering (per unit space) for MB amounts to 0.6%. MB may be thought of as 'noise' fields in which the microbreakings exist.

As to radiothermal models of foam systems, detailed laboratory and theoretical investigations, carried out under the guidance of the author of this book during the period of 1974–1981, have shown that there exist two contrasting classes of foam systems – the emulsion monolayer and the layer of foam of polyhedrous structure (Militskii *et al.*, 1978). In this case it was strictly demonstrated (Raizer and Sharkov, 1981), that the electrodynamical models of a homogeneous or inhomogeneous dielectric layer, with parameters corresponding to a heterogeneous mixture of water and air (Matveev, 1971), do not exhibit a quantitative agreement with the experiment. The same is true for the models of a discrete stratified medium (Williams, 1971; Stogryn, 1972; Rozenkranz and Staelin, 1972; Tang, 1974; Bordonskii *et al.*, 1978; Smith, 1988) and for the models of a smoothly varying transition dielectric layer (Bordonskii *et al.*, 1978). The electromagnetic properties of coarse-disperse media in the microwave band are most completely reproduced by continuous stratified-inhomogeneous models with strict allowance for diffraction properties of hollow spheres and hexagonal structures, with allowance for a blurred interface boundary between the disperse structure and the water surface and with allowance for the depth inhomogeneity of a dielectric layer (Raizer and Sharkov, 1981). Slightly simplifying the situation, one can say that the matter is as follows. For the electromagnetic range under consideration the hollow water spheres (or the hexagonal structures) represent some kind of small black bodies, which intensively absorb the electromagnetic energy owing to inter-bubble diffraction. The complete consideration of these issues is beyond the framework of the present book, and so, we can recommend the reader to consult the original literature (Raizer and Sharkov, 1981).

12.5 MICROWAVE REMOTE SENSING OF CATASTROPHIC OIL SPILLS ON THE SEA SURFACE

As a quite instructive example of the efficient use of microwave radiothermal instruments, along with active microwave means, we shall briefly describe the results of remote study of the evolution of catastrophical oil spills on the sea surface in regions of intensive oil output on the continental shelf. These investigations were carried out by the specialists of the Space Research Institute (Moscow) in 1976–1977 (Bespalova *et al.*, 1978, 1983).

The problem of the interaction of oil pollutions with a sea medium is significant in ecological and physical investigations of the ocean (Scott, 1978, 1999; Scott and Thomas, 1999). The main tasks in studying this problem are: the determination of sources and scales of pollutions, the estimation of thickness and volume of the oil layer as well as of spatial and temporal variability of oil slicks; the monitoring of further evolution of oil–water conglomerates and of the procedure of self-purifying of a sea medium.

The means of perspective remote sensing that allow one to approach the solution of these problems include side-looking radar (SLR) (Kalmykov, 1996), synthetic aperture radars (SAR) (Johannessen *et al.*, 1994) and radiothermal systems (Bartsch *et al.*, 1987). Using such instruments installed onboard flight vehicles, it is possible to measure, for a comparatively short time, the distribution of a specific cross-section of backscattering and radiobrightness fields over a considerable sea surface area. However, one should bear in mind that the physical reasons causing the appearance of contrasts in radiobrightness and backscattering fields can be quite different, and, therefore, the informative capability of these remote sensing data will also be mutually complementary. This section presents the experimental results of studying the spatial–temporal variability of wave-driven sea surface pollution by oil products in the region of Neftyanye Kamni (Oil Rocks) shoal (the Caspian Sea area), resulted from catastrophic oil spill under various hydrometeorological conditions. These studies were carried out from November 26 till December 1 1976, and from November till December, 1977. Unlike earlier works, these remote sensing experiments were performed using passive and active sensing means disposed on various carriers simultaneously. The latter means included the two-polarization centimetre-band 'Toros' SLR installed on the Russian An-24 aircraft, which was used earlier in geological and glaciological investigations. The passive remote sensing system included the multifrequency radiothermal radar instruments installed on board the Russian Il-18 aircraft laboratory (Amirkhanyn *et al.*, 1975).

12.5.1 Investigation techniques and processing of the results

The techniques of performing and processing the results of a complex radiophysical experiment were as follows. The radar investigations were carried out simultaneously in two separate vertical–vertical (VV) and horizontal–horizontal (HH) channels. The flights were accomplished at the altitude of 1500 m by flying around the investigated sea area in the 'rectangular approach traffic pattern'. Since the radar image in the

pollution zone was virtually homogeneous and did not contain any clearly discernible details (see Figure 12.15), the further analysis of the radar data was performed from planimetric representations of radar images (the planimetric map-schemes, Figure 12.16). The procedure of aircraft radiothermal experiments was as follows. The flights were accomplished at an altitude of 200 m with a velocity of 360 km/hour directly above the investigated water area with tacks intersecting at a particular, preselected point over a stable geographical landmark (a 'sprocket'). The results of radiothermal experiments are presented in the form of radiothermal map-schemes (Figure 12.17), where solid lines represent the levels of equal radiobrightness temperature (radio-isotherms). The technique of plotting radio-isotherms corresponds to the well-known rules of constructing synoptic maps in meteorology. The time of committing the flights over a full 'sprocket' or over of part one (from 1.5–2 hours to 0.5 hours) was accepted as a period of averaging the picture of hydrometeorological phenomena of corresponding scale.

12.5.2 Analysis of radar mapping data

The basic mechanism of radar signal backscattering by the sea surface is resonance Bragg scattering. For horizontal polarization at low view angles the scattered signal is mainly also formed, except for the Bragg mechanism, by signal reflection from the ridges of large waves before their breaking. The analysis of radar images obtained indicates that the signal splashes, caused by such reflections, are clearly seen over the whole swath width, that is, at incidence angles of 4–20° (Figure 12.15). The appearance of oil on the sea surface causes changes in radiowave backscattering for several reasons, the most essential of which is the suppression of high-frequency components of the spectrum of gravitation-capillary waves owing to sharp changing of attenuation with the appearance of the oil film on the sea surface. Figure 12.16 presents the contour map-schemes obtained from the positives of the VP (vertical polarization) channel, on which the evolution of considerable oil pollutions during 7 hours on November 26, 27 and 28, 1976 was recorded. The hydrometeorological situation on the night and morning of November 26 1976, was characterized by a steady north-east wind disturbance (3 points) against the background of swell from the north and north-east wind (5 m/s) at the sea surface state (SSS) of 2 points (Beaufort notation). The character of pollutions in the morning of November 26 1976, represents a vast uniform field of irregular shape with broad 'sleeves' elongated in the south-west direction. In general, the shape of the field was formed, apparently, under the effect of the north-east wind and seaway, which had existed during the hours of the night and morning. From about midday on the area of a spot began sharply to contract and divide into separate fields and bands, and by about 17 h 30 m the spot had virtually disappeared. This process was promoted by a drastic change of meteorological conditions – the north wind strengthening up to 12 m/s and wind disturbance increasing up to 4 points (the SSS was evaluated as 4 points). Thus, the total 'lifetime' of a vast oil slick amounted to 5 hours, and, supposing the exponential law of decay under natural conditions, the spot 'half-life' period, recorded by a radar, equals 1–1.5 hours under the given hydrometeorological conditions,

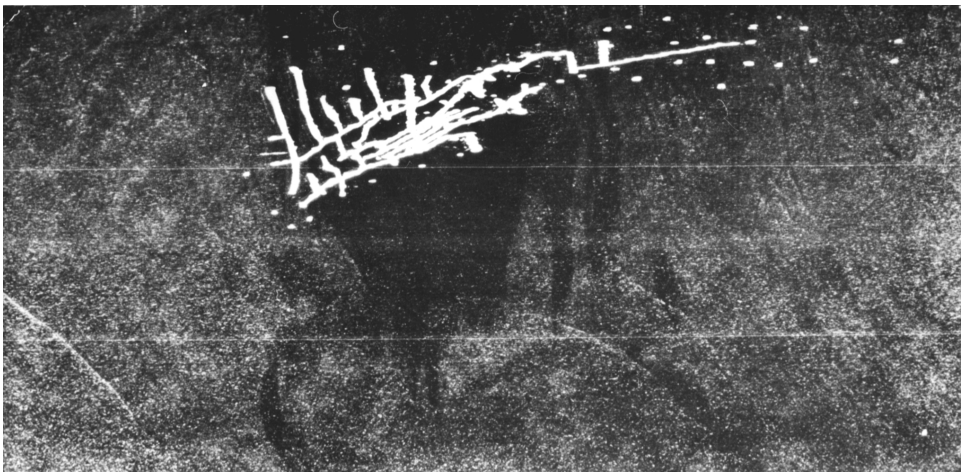

(a)

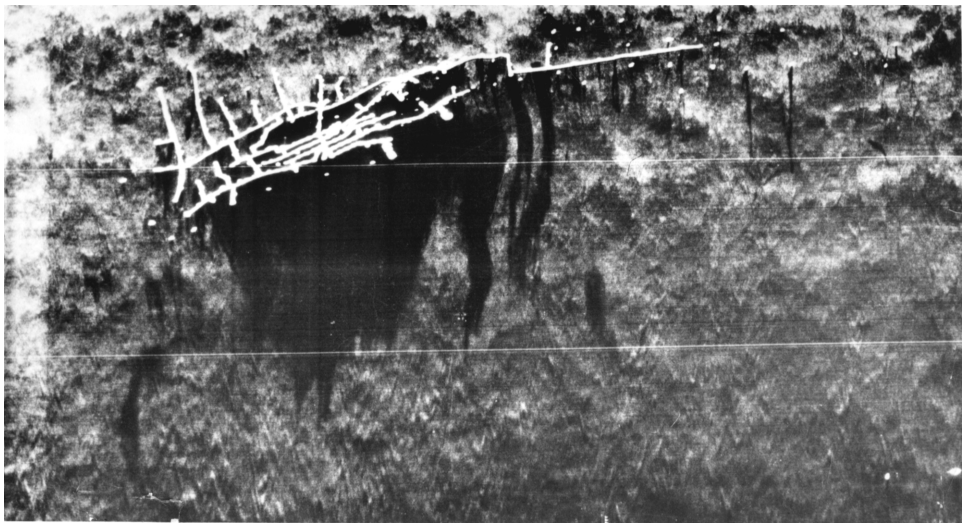

(b)

Figure 12.15. Backscattering images of a rougt sea surface obtained by side-looking radar 'Toros' (Russian research airplane AN-24) for the horizontal–horizontal (a) and vertical–vertical (b) polarization regimes in the presence of oil pollution near the 'Oil Rocks' oil installation (the Caspian Sea). Date of flight experiment was 26 November 1976. Black fields correspond to oil spills. The bright line system standing out sharply against the sea backscattering signal corresponds to the backscattering signal from the scaffold bridges of the oil installation.

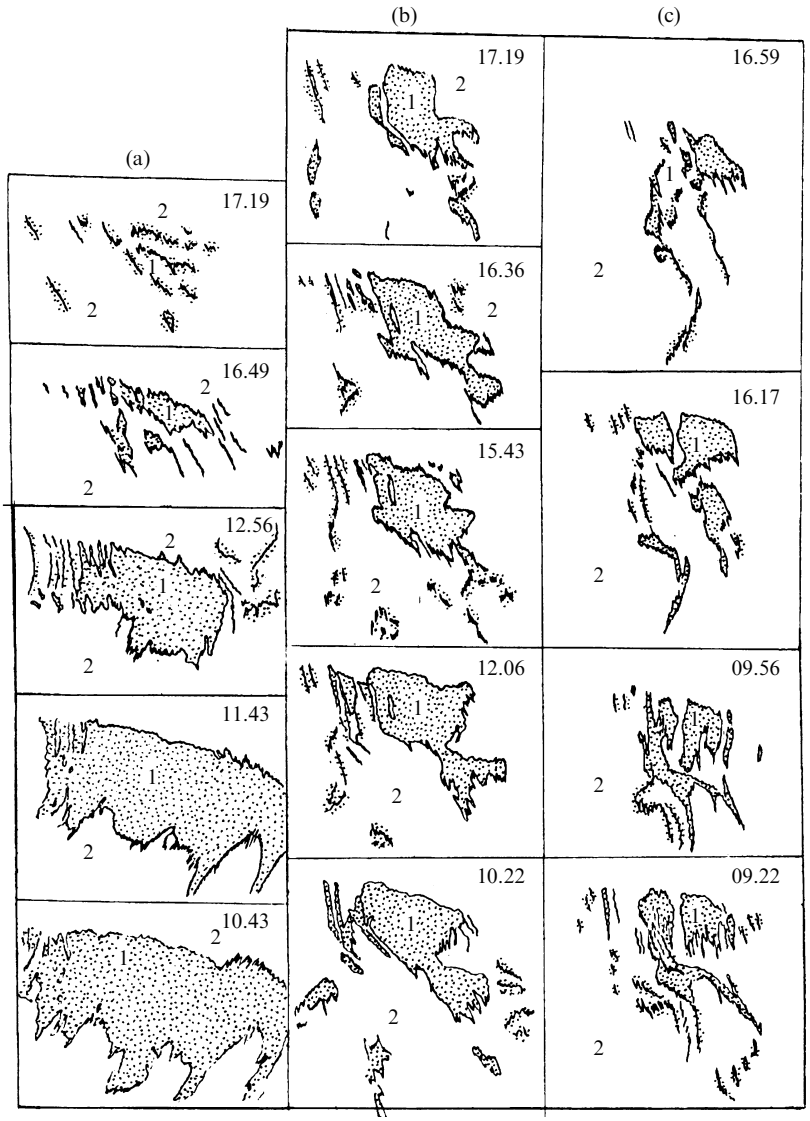

Figure 12.16. The spatial–temporal evolution of catastrophic oil spills presented by a temporal series of schematic maps of the backscattering images. (1) Oil spill fields; (2) rough sea surface without oil pollution. (a) Date of the experiment was 26 November 1976 from 10.43 (Moscow time) till 17.19. The surface wind speed and direction was 12 m/s and 360°. Sea state was 4 on the Beaufort scale. (b) Date of the experiment was 27 November 1976 from 10.22 (Moscow time) till 17.19. The surface wind speed and direction was 9 m/s and 360°. Sea state was 4 on the Beaufort scale. (c) Date of the experiment was 28 November 1976 from 09.22 (Moscow time) till 16.59. The surface wind speed and direction was 12 m/s and 360°. Sea state was 4 on the Beaufort scale. Figures in each scheme present the Moscow time of experimental image.

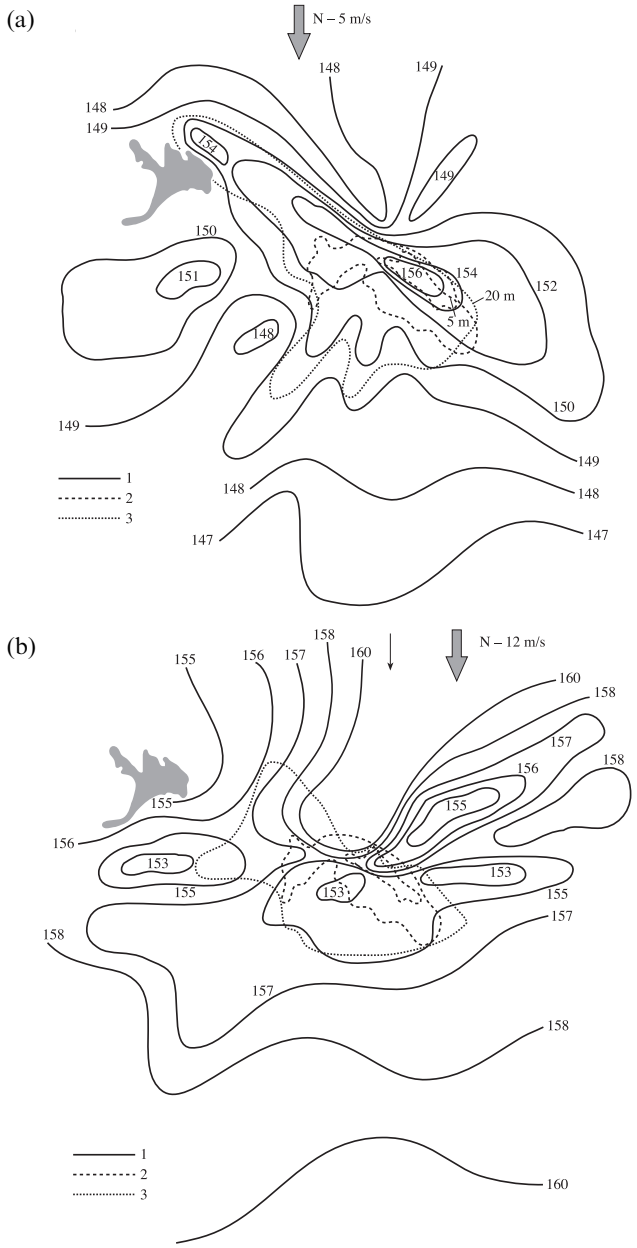

Figure 12.17. Radio-emission isothermal maps of the sea surface studied at wavelength 8 mm (26 November 1976): (a) radio map was performed during time from 09.35 till 11.30 (Moscow time); (b) radio map was performed during time from 13.35 till 15.55 (Moscow time). 1, radio isotherms (figures present absolute values of brightness temperature); 2, bathymetry data (m); 3, areas where an aircraft operator observed oil pollution. The heavy black arrows show the direction of the surface wind speed vector.

whereas in the laboratory conditions this value varies from 6 to 100 hours for an oil film.

The oil pollution on the morning of November 27 1976, appeared as a patchy formation of considerable area (and some small-size slicks) stretching in a south-east direction and formed by the north wind and a fairly strong undersea flow, which prevailed during the night, morning and day of November 27. Of interest is the fact that, despite a fairly heavy sea (4–5 points) and wind (8–9 m/s), the oil slick area has only slightly varied throughout the day of November 27. And only small areas of slick were carried away 15–20 km south-eastward. This is, apparently, explained by the fact, that oil had continued to leak from the source all this time.

The oil pollution of November 28 consisted of separate bands and spots stretching in a south-east direction; the extension of this area was 15–18 km. As a whole, the system of slicks only slightly varied up to 16 h 17 m and then began quite sharply to decrease.

12.5.3 Radiothermal measurement data analysis

The radiothermal investigation of oil pollution, carried out within a wide band of frequencies directly in the region of carrying out the experiments, made it possible to clearly reveal two effects arising at the interaction of the developed seaway with the film of oil products. One of the effects (the positive variations from 2 K at wavelength of 3 cm to 10 K at wavelength of 0.8 cm for a seaway of 1–2 points) is physically associated with the phenomenon of coordinating the wave resistances of two half-spaces – air and water – by the oil film (Figure 12.18). The second effect, observed at a seaway of 4–5 points (the negative variations relative to the radiobrightness of a non-disturbed background from -1 K at wavelength of 3 cm to -5.5 K at wavelength of 0.8 cm), is determined by suppressing the gravitation-capillary components (a ripple) of the seaway spectrum, drop-spray clouds and foam activity by the oil film (Figure 12.19). Both in the first and in the second case the spectral dependencies within the limits of wavelengths of 0.8–3.2 cm had the monotonous, nearly hyperbolic character of variation magnitude decreasing when the working wavelength increases (Figure 12.20).

Thus, radiothermal multifrequency measurements allow one to determine, under the indicated hydrometeorological conditions, the thickness of oil films (with corresponding spatial averaging). The radar mapping of the mentioned water area region (50×50 km), carried out over the days of the described experiments, made it possible to reveal the complicated spatial structure of the radiothermal field in this region. This structure included the zones of both heightened ('warm') and lowered ('cold') radiobrightness values (with respect to the background brightness), caused by the presence of visually detected pollution, as well some peculiar zones of negative 'radio shadow' and the 'warm' zones of a lobe-type structure. The characteristic radiomap-schemes are presented in Figure 12.17. For example, the radiomap of November 26 1976, for the time window of 9 h 35 m Msk to 11 h 30 m Msk had a 'warm' region (in the 0.8-cm channel), stretched from the south-east towards the north-west and corresponded, in general, to a visually observed pollution area. One

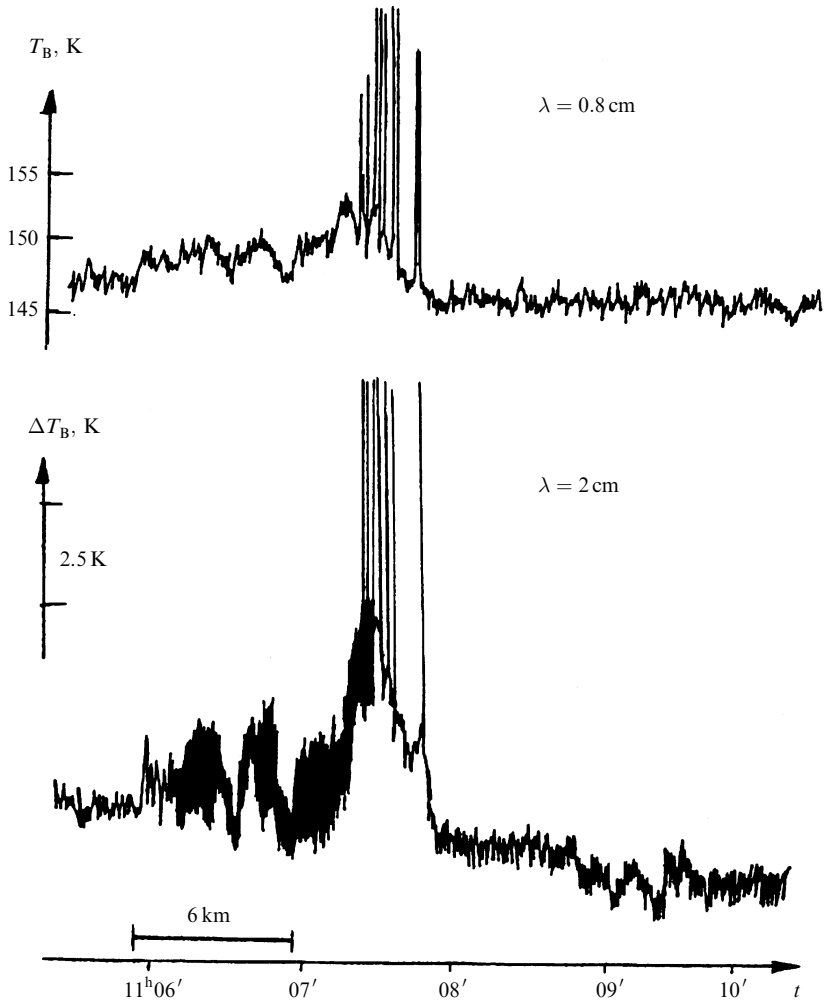

Figure 12.18. Fragments of synchronous output signals of airborne radiometers R2 and R0.8 when crossing an area under study. The working area is near the 'Oil Rocks' oil installation (the Caspian Sea). Date of flight experiment was 26 November 1976. ($H = 400$ m.) The surface wind speed and direction was 5 m/s and 45°. Sea state was 2 on the Beaufort scale. Temperatures of water and air were 12.2°C and 9.1°C. Moscow time, spatial scale and indoor temperature calibration are shown on the abscissa and on the ordinate. The strong linear variations standing out sharply against the sea emission signal correspond to the emission signal from the scaffold bridges of the oil installation.

should also pay attention to the presence of heightened (by 3–4 K as compared to the background) radiobrightness zones stretching out 10–15 km in the east and west directions and looking like lobes. The oil pollution on the sea surface is not visually observed in these regions, and the mentioned changes of radiobrightness

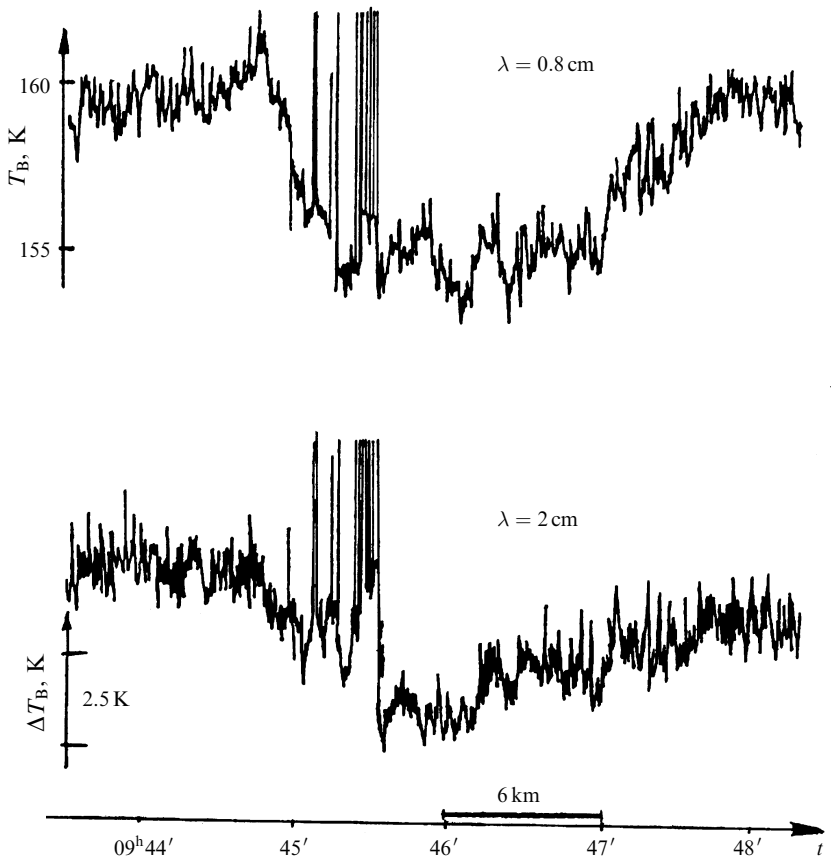

Figure 12.19. Fragments of synchronous output signals of airborne radiometers R2 and R0.8 when crossing an area under study. The working area is near the 'Oil Rocks' oil installation (the Caspian Sea). Date of flight experiment was 27 November 1976. ($H = 400$ m.) The surface wind speed and direction was 10 m/s and 360°. Sea state was 4 on the Beaufort scale. Temperatures of water and air were 10.2° and 8.2°C. Moscow time, spatial scale and indoor temperature calibration are shown on the abscissa and on the ordinate.

should be attributed to the increase of energy of gravitation-capillary components in the seaway spectrum. The analysis has shown that the radio image in the 2-cm channel corresponds, in general to the features of the radiomap obtained in the 0.8-cm channel. During the experiment the meteorological conditions sharply changed at the middle of the day: the wind strengthened up to 10–12 m/s, the northerly wind disturbance achieved 4 points, the SSS was estimated by 4 points. The flight took place from 13 h 55 m to 15 h 55 m. The aforementioned regime should be considered unsteady, since the time of the wind disturbance 'tuning' exceeds 3–4 hours. The radiopattern in the 0.8-cm channel (Figure 12.17(b)) underwent considerable changes: the radiobrightness of the sea background far from the region under

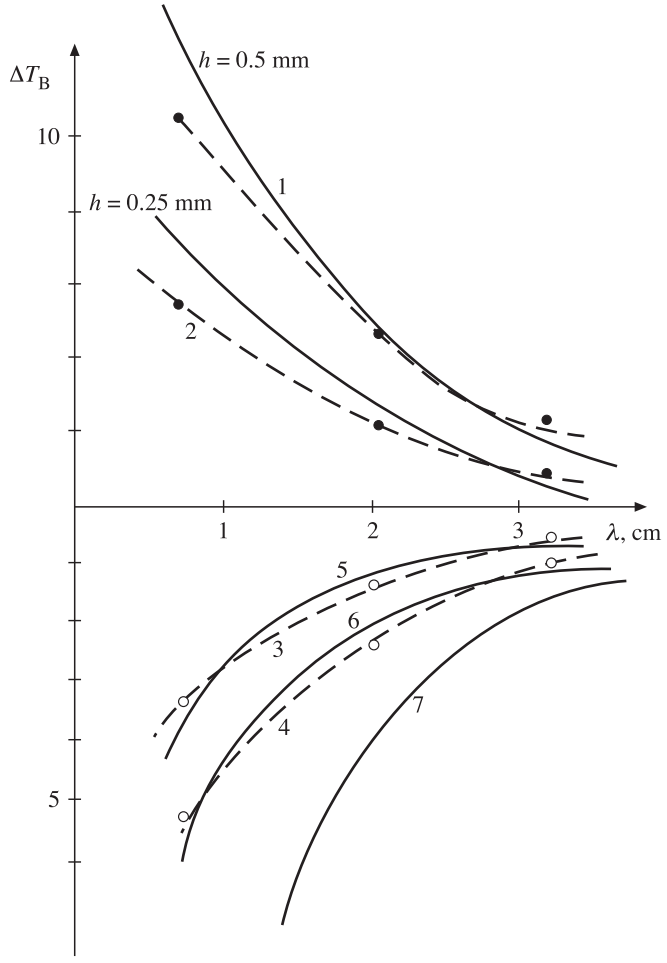

Figure 12.20. Experimental spectra of radiobrightness temperature variations against the pure (non-pollution) sea emission signal at three frequency channels (wavelengths 0.8, 2 and 3 cm) obtained at the same place on the sea surface: (a) positive variations (black points and broken curves) for weather conditions of 26 November 1976; (b) negative variations (circles and broken curves) for weather conditions of 27 November 1976. See figures and solid curve notation in the text.

study was now 159–160 K; that is, it increased by 10–11 K. An interesting feature of the considered radio images is the presence of a peculiar negative 'radio shadow' area to the south of the centre of the investigated area. The dimensions of the 'shadow' area were: 14–16 km in the southerly direction and 30–35 km in the east–west direction; the negative deviation from the sea background radiobrightness value (159–160 K) was quite small (2–4 K). This area is most clearly displayed in the 0.8-cm channel.

Considerable wind and seaway strengthening during the night from November 26 to 27 1976 (wind of 14 m/s and seaway of 5 points) distorted the picture of the oil pollution – the oil film was broken into local sections, which were carried away 15–20 km southward from the investigated region. In spite of this circumstance, the features of the radiopattern of November 27 corresponded, in general, to those obtained on the previous day. An important feature of the results considered is the experimentally detected rapid variability of radiothermal fields of the non-stationary seaways (the 'radio shadow' area). Here it should be noted that the velocity of evolution of such fine features of the radiothermal field (with variations of 0.5–2 K) is considerable, and the order of its magnitude corresponds to the order of the wind speed (in the case under consideration the rate of evolution of radio image details can be estimated as 3–7 m/s). This implies that to produce an 'instantaneous' radiopattern separating fine features of the radio fields of sea water areas of the order of 50×50 km the observation time should be less than 3–5 minutes, which is only made possible by using an airborne or spaceborne radiothermal surveying system.

12.5.4 Joint analysis of radar and radiothermal images

Combined radiothermal and radar map-schemes in the same scale and with approximately the same resolution element of 50–100 m are shown in Figure 12.21. Analysis of these maps (of November 26 1976) in the 0.8-cm channel and from radar observations, as well as of the dependencies of the averaged (in the resolution element) of the oil film thickness at the AOA, BOB cross-sections (Figure 12.21) allows one to conclude that there is a rather complicated internal structure to the oil slick. A characteristic feature of the pollution area is the existence of at least three zones. The first one represents a fairly stable 'hot' core with an area of about 4% of the total area of the slick, where 10% of the total oil mass is concentrated, and where, apparently, the source of pollution itself is localized. (According to the radar data, this source has continued to leak oil until 12 h 00 m, as seen from the beginning of analysis.) With increasing distance from the core southward, that is, in the direction of action of the wind and seaway, the second zone is observed – the rapid drop of film thickness (the spreading process). And then the third zone appears – the long 'plateau' occupying 70% of the total slick, with a slow change of film thickness from 0.1 mm and below, where, apparently, the process of evapouration occurs. More than 52% of the total oil mass is concentrated in the 'plateau' zone. Figure 12.22 gives a visual idea of the distribution of averaged thickness, h, over the AOA cross-section (curve 1) and over the BOB cross-section (curve 2). The same figure shows the oil slick boundaries, which are seen on the radar image (the radar for cross-section AOA and the radar for cross-section BOB). The comparison of radar and radiothermal data gives an estimate of the oil film thickness near the spot boundary, seen on radar images, as 20–40 micrometre. Figure 12.23 presents the results of superposition of schemes of four types of observations on December 1 1977: radar, radiothermal-radar, aerial photography and visual (the onboard observer), as well as the fragments of registograms in the 0.8-cm channel. The analysis of such a

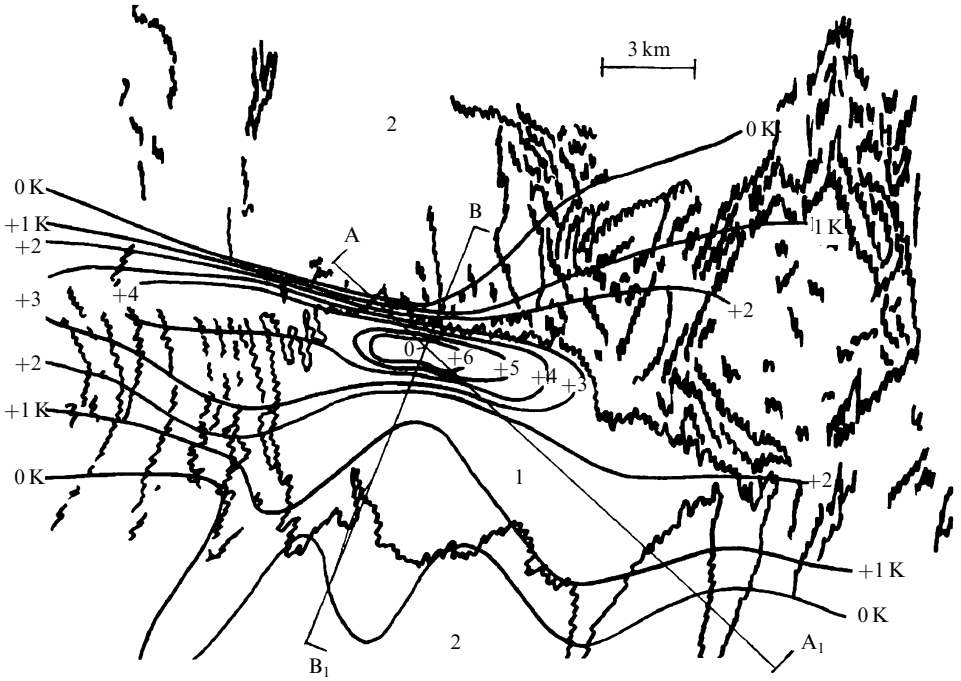

Figure 12.21. SLR schematic map (26 November 1976, 11.43 Moscow time) combined with fragments of the radio-emission isothermal map (9.30–11.30 Moscow time) of sea surface under study at wavelength 8 mm: 1, sea area polluted by oil spill with SLR data; 2, pure sea surface. Solid lines are radio isotherms. Figures are relative variations of radiobrightness temperatures. AOA_1 and BOB_1 are cross-sections under study.

superposition indicates that the results of radar, visual and aerial photography observations, in general, coincide well in detecting the oil spot boundaries. At the same time, the radiothermal-radar observations reveal the 'radio-shadow' features, which cannot be recorded by radar and other observation techniques.

12.5.5 Radiospectroscopic observations

To reveal in more detail the physical features observed in wave-driven sea surface pollution by oil, in Figure 12.20 the spectrum of radiobrightness temperature variations is constructed from the synchronous data of three frequency channels (0.8, 2 and 3 cm), recorded virtually at the same IFOV (with an accuracy of spacing the axes of the antenna directional patterns of about 15–20 m). The upper part of the figure shows the experimental frequency dependencies (the dotted line) of positive variations in the intensive pollution regions (on November 26 1976), just by the oil production ramps (curve 1) and 4 km southward from the ramps (curve 2). On the same figure are plotted the spectral curves (solid lines) of radiobrightness variations (relative to the quiet water surface), calculated within the planar-stratified

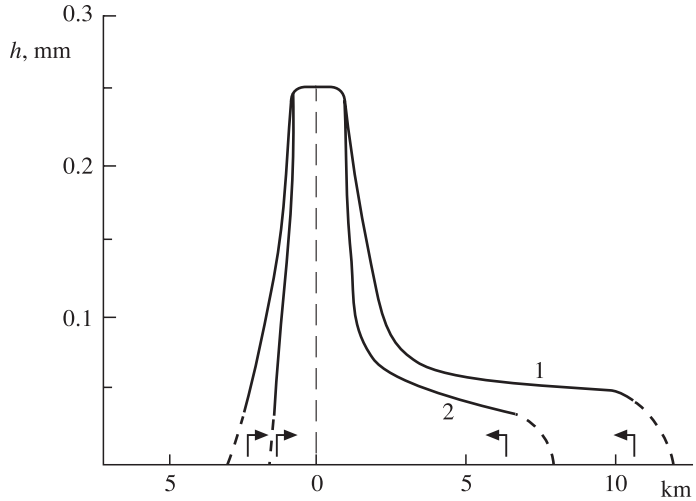

Figure 12.22. The spatial distribution of averaged oil film thickness over AOA_1 (curve 1) and over BOB_1 (curve 2) cross-sections. Arrows show the boundaries of backscattering images over AOA_1 and BOB_1 cross-sections.

model framework (Chapter 7) for two values of thickness of oil film on the water surface: 0.25 and 0.5 mm. As to the considered region of positive variations, the comparison of calculated and experimental spectra of radiobrightness variations indicates that, under the given hydrometeorological conditions and at the given level of generalization (a spatial resolution of 10–15 m) the planar-stratified model rather well explains, in general, the experimental data obtained. This makes it possible to estimate the thickness of a surface film of oil products and the total volume (or tonnage) of oil spreading after radio-mapping. The lower part of Figure 12.20 presents the experimental frequency dependencies (the dotted line) of negative variations in the Neftyanye Kamni (Oil Rocks) region (on November 27 1976) just by the oil production ramps (curve 3) and 1 km southward of the ramps (curve 4). The frequency dependencies have a monotonous, nearly hyperbolic character of decreasing value of negative variations with increasing working wavelength. The characteristic wavelength dependence of the radiobrightness spectrum variations gives an idea of its considerable contribution to the effect of suppressing drop-spray clouds by the oil film (see Chapter 10). Figure 12.20 presents the calculated dependencies of drop-spray clouds radiation (curves 3 and 4), which are plotted in such a manner that they coincide with the experimental dependencies at the wavelength of 2 cm. By the same formula it is possible to estimate, using the experimental data, the values of densities for the spray layer heights of 10 and 100 cm. These densities were found to be $C = 2 \times 10^{-3}$ for the first case and $C = 2 \times 10^{-4}$ for the second one. In other words, these values were quite close to those experimentally observed under similar seaway conditions. It is of interest to evaluate the frequency dependence of radiobrightness variations, caused by the appearance of a small transition layer 1 mm thick with dielectric parameters variation according to the

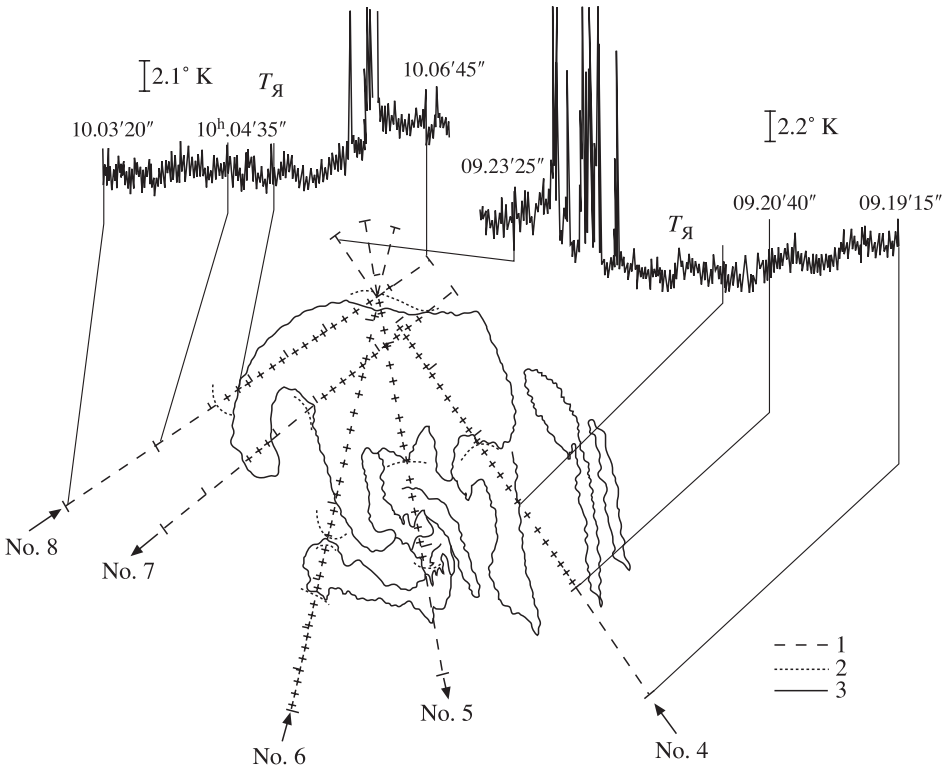

Figure 12.23. Schematic superposition of observing data from four types of sensing of oil pollution area (1 December 1977): by aerial photography (1), visual observation (2), radar (3) and radiometer (wavelength 0.8 cm). Radiothermal data was represented as temporal recordings. Figures and arrows near flight paths present their numbers and directions.

hyperbolic tangent law, and, thus, to simulate, in a certain sense, the radio-emission of a ripple on a large-size wave. The corresponding computer calculations on multi-layer software (Chapter 7) are reflected by curve 7. It can be seen that the wavelength dependence is essentially stronger, than λ^{-1}. Therefore, it is less reliable to explain the indicated effects by suppression of the fine-structural dielectric transition by the oil film than by suppression of drop-spray clouds.

To finally reveal the physical reasons for the origin of negative variations of radiobrightness of the wave-driven sea surface in the presence of oil pollution, it is necessary to expand the set of frequencies in remote sensing measurements.